RPA Mediates Recruitment of MRX to Forks and Double-Strand Breaks to Hold Sister Chromatids Together

A Seeber, Am Hegnauer, N Hustedt, I Deshpande, J Poli, J Eglinger, P Pasero, H Gut, M Shinohara, Kp Hopfner, et al.

RPA-mediated recruitment of MRX to forks and double-strand breaks holds sister chromatids together

Andrew Seeber[1,2], Anna Maria Hegnauer[1], Nicole Hustedt[1,3], Ishan Deshpande[1,2], Jérôme Poli[1], Jan Eglinger[1], Philippe Pasero[4], Heinz Gut[1], Miki Shinohara[5], Karl-Peter Hopfner[6], Kenji Shimada[1] and Susan M. Gasser [1,2]*

Total characters incl spaces = 56838 without fig legends/ 8362 in fig legends (65220 total)

1) Friedrich Miescher Institute for Biomedical Research, Maulbeerstrasse 66, CH-4058 Basel, Switzerland.

2) University of Basel, Faculty of Natural Sciences, Klingelbergstrasse 50, CH-4056 Basel, Switzerland

3) current address: The Lunenfeld-Tanenbaum Research Institute, Mount Sinai Hospital, 600 University, Avenue, Toronto, Canada

4) Institute of Human Genetics, CNRS UPR 1142 Montpellier, France

5) Institute for Protein Research, Osaka University, Suita, Osaka 565-0871, Japan

6) Gene Center LMU Munich, Feodor-Lynen Str. 25, 81377 Munich, Germany

* Lead author: Tel: +41 61 697 7255; Fax: +41 61 697 3976

Email: susan.gasser@fmi.ch

Running title: RPA-MRX interaction links sister chromatids

Key words: Mre11, Rad50, Xrs2, Replication Protein A, sister chromatids, Mec1 checkpoint

Summary

The Mre11-Rad50-Xrs2 (MRX) complex is related to SMC complexes that form rings capable of holding two distinct DNA strands together. MRX functions at stalled replication forks and double-strand breaks (DSB). A mutation in the N-terminal OB-fold of the 70-kD subunit of yeast replication protein A, *rfa1-t11,* abrogates MRX recruitment to both types of damage. The *rfa1* mutation is functionally epistatic with loss of any of the MRX subunits for survival of replication fork stress or DSB recovery, although it does not compromise end resection. High resolution imaging shows that either the *rfa1-t11* or the *rad50Δ* mutation lets stalled replication forks collapse, and allows the separation not only of opposing ends, but of sister chromatids at breaks. Given that cohesin loss does not provoke visible sister separation as long as the RPA-MRX contacts are intact, we conclude that MRX also serves as a structural lynchpin of sister chromatids at breaks.

Introduction

Eukaryotic genomes incur damage continually from both exogenous and endogenous insults. The DNA damage and intra-S phase checkpoints are important response mechanisms that allow cells to deal with damage both by arresting the cell cycle when necessary, and by activating the appropriate repair machinery (Ciccia and Elledge, 2010; Harrison and Haber, 2006; Hustedt et al., 2013). Central to the checkpoint response are the conserved checkpoint kinases Mec1-Ddc2 (ATR-ATRIP) and Tel1 (ATM). Importantly, the trimeric complex that binds single-strand DNA (ssDNA), replication protein A (RPA), acts as a recruitment platform for checkpoint and repair proteins, including but not limited to Mec1-Ddc2 and the Tel1 activator, Rad9, both at stalled forks and at DNA double-strand breaks (DSB) (Paciotti et al., 2000; Rouse and Jackson, 2002; Xu et al., 2008; Zou and Elledge, 2003). The failure of RPA to coat ssDNA results in replication catastrophe in S phase, and compromises homologous recombination (HR), underscoring the crucial role of this complex (Hustedt et al., 2013; Toledo et al., 2013). While checkpoint activation coordinates cell cycle events, the maintenance of the physical structure of a stalled fork or a DSB is also crucial for repair through pathways that depend on recombination with a sister chromatid (Bjergbaek et al., 2005; Petermann and Helleday, 2010; San Filippo et al., 2008; Wang et al., 2004)**.**

Structural maintenance of chromosomes (SMC) complexes are central to long-range chromatin organization, and are required for the proper meiotic segregation of replicated DNA, for chromosome condensation and homology-based DNA repair (Uhlmann, 2016). SMC proteins are characterized by a distinct coiled-coil domain that contains a hinge, allowing the coil to fold back on itself, bringing the N- and C- terminal globular domains together (Hirano, 2006). The

best characterized SMC protein complex is cohesin, which comprises two SMC proteins, Smc1/3, and two non-SMC proteins, Scc1 (Mcd1) and Scc3. The latter serve as a clasp to bridge the head domains of Smc1/3. This complex keeps sister chromatids paired, particularly in G2 and prometaphase (Uhlmann et al., 1999). Cohesin is also recruited to DSBs and stalled replication forks where it contributes to repair (Heidinger-Pauli et al., 2008; Strom et al., 2007; Strom and Sjogren, 2007; Unal et al., 2004) and replication fork recovery (Tittel-Elmer et al., 2012).

The Mre11/Rad50/Xrs2 (MRX) complex is structurally similar to cohesin and is often characterized as the first responder to a DSB (Lisby et al., 2004). MRX promotes the initiation of end-resection with the co-factor Sae2 (CtIP) (Garcia et al., 2011; Lengsfeld et al., 2007; Mimitou and Symington, 2008; Williams et al., 2009). While abundant data implicate MRX in checkpoint activation, telomere elongation and initiation of resection (reviewed in Stracker and Petrini, 2011; Lafrance-Vanasse et al., 2015), only a few studies have asked whether it plays a structural role at damage. Supporting this, it was shown that the two sides of a DSB separate from each other in ~12-15% of cells lacking MRX (Kaye et al., 2004; Lobachev et al., 2004; Williams et al., 2008). MRX is thought to form a dimer complex with two Rad50 subunits, which like Smc1 and Smc3 in cohesin, have long coiled-coil arms that can stretch up to ~ 600 Å (de Jager et al., 2001a; Hopfner et al., 2002; Moreno-Herrero et al., 2005). These coiled-coil arms can dimerize at their tips through a zinc hook domain, allowing the formation of ring-like structures or higher-order oligomers that could hold two DNA molecules together (de Jager et al., 2001b; Hopfner et al., 2002). Functional studies showing that the hook domain is essential for MRX function in DNA repair, telomere maintenance, and meiotic DSB formation (Hohl et al., 2015;

Wiltzius et al., 2005), are consistent with this hypothesis, but do not prove it. Genetic data also implicate MRX in the repair of DSBs by sister chromatid exchange (Gonzalez-Barrera et al., 2003; Hartsuiker et al., 2001).

Our study starts from the discovery of an epistatic relationship between a point mutation in the large subunit of RPA, *rfa1-t11,* and null alleles of *MRE11*, *RAD50* or *XRS2*, under conditions of replication stress in *S. cerevisiae*. The *rfa1-t11* allele bears a single point mutation (K45E) in the N-OB fold of Rfa1, which renders the strain deficient for both mitotic and meiotic recombination, although end-resection occurs normally (Dubrana et al., 2007; Umezu et al., 1998). We show here that *rfa1-t11* fails to stabilize stalled replication forks, leading to fork collapse. This effect is not due to an impaired activation of the S-phase checkpoint. Rather, *rfa1-t11* reduces the recruitment of MRX to both stalled replication forks and DSBs *in vivo*, resulting in an inability to restart stalled forks and end separation at DSBs. We show that Rfa1 and MRX interact in an *rfa1-t11*-sensitive manner *in vitro*. Finally, we find that MRX holds sisters and break ends together in an RPA-dependent manner at DSBs *in vivo*, even when cohesin is inactivated. These findings argue for a novel structural role for MRX at stalled replication forks and breaks.

Results

The rfa1-t11 K45E *mutation disrupts a basic patch in the N-OB binding pocket of Rpa70/Rfa1*

The ssDNA binding protein RPA, is composed of three subunits, all of which are essential for cell viability in budding yeast (Fig. 1A). The largest subunit (*Sc*Rpa70 or Rfa1) contains 4 OB-fold domains, three of which are implicated in ssDNA binding, while the N-terminal OB-fold serves as a recruitment platform for other proteins involved in replication stress and DSB repair. This

domain was reported to bind a number of proteins including Ddc2/ATRIP, Sgs1 and Rad9 in budding yeast, and p53 in mammalian cells (Ball et al., 2007; Bochkareva et al., 2005; Dutta et al., 1993; Flynn and Zou, 2010; Hegnauer et al., 2012; Xu et al., 2008).

RPA was extensively mutagenized to isolate non-lethal mutations that were subsequently used to identify binding partners and domain-specific functions (Binz and Wold, 2008; Umezu et al., 1998; Zou et al., 2006). A previously characterized mutation, *rfa1-t11* (K45E), was reported to be specifically defective in HR, while supporting normal DNA replication (Kanoh et al., 2006; Wang and Haber, 2004). This lysine to glutamate charge reversal maps to the binding pocket of the N-terminal OB fold. Intriguingly, it confers recessive sensitivity to hydroxyurea (HU), an agent that induces replication stress by depleting dNTP pools (Fig. S1A), although without HU there was no delay in S-phase entry: replication forks fire and progress without pausing or forming aberrant recombination intermediates (Fig. S1BC).

To understand the structural effect of the K45E substitution, we expressed, purified and crystallized the mutant N-terminal OB fold of yeast RFA1 (aa 1 – 132), and resolved its structure to 1.8 Å (Fig. 1B, Table 1) using the single-wavelength anomalous diffraction method (Supplemental Exp. Procedures). Indeed, the *rfa1-t11* mutation disrupts a basic patch in the binding pocket of the N-terminal OB fold, as the mutant residue protrudes into the binding cleft. Given that the ligands of this domain are acidic, one predicts that this K45E mutation interferes with protein-protein interactions that are important at stalled forks.

Earlier reports suggested that the N-terminal OB domain is responsible for the recruitment of ATRIP/Ddc2 to ssDNA, and activation of the ATR kinase (Rouse and Jackson, 2002; Zou and

Elledge, 2003). Mec1/Ddc2 is responsible for the vast majority of Rad53 phosphorylation induced by replication stress (Hustedt et al., 2013). Therefore, we tested for defects in checkpoint activation on a synchronized population of *rfa1-t11* cells, after releasing from G1 arrest into 0.2M HU for 90 min. Rad53, however, was efficiently activated in the *rfa1-t11* mutant, showing a pronounced shift in electrophoretic migration (Fig. 1C). A similar assay in a strain bearing *rfa1-t11* combined with *tel1Δ* showed no change, arguing that Rad53 activation on HU is primarily mediated by Mec1 (Fig. S1D). In any case, impaired Mec1 kinase activation is not responsible for the *rfa1-t11* mutant's sensitivity to HU.

MRX and rfa1-t11 show similar E-MAP patterns in response to replication stress

One means to identify a mutant's pathway of action, is to compare epistatic growth profiles obtained by combinatorial pairing of mutant alleles. We therefore performed an epistatic miniarray profile (EMAP) to compare the growth of *rfa1-t11* and 34 other query strains crossed to 1311 deletion strains or Decreased Abundance by mRNA Perturbation (DAmP) alleles, grown either in 0, 20 or 100 mM HU (Hustedt et al., 2015). This resulted in a gene network of 45885 interactions that had either synergistic or suppressive effects, or failed to grow altogether on HU (Figs. 1A, S2AB). One can correlate the patterns of sensitivity to identify genetic pathways affected similarly by specific mutants, because mutants that share phenotypic correlations often share functionality (Morrison et al., 2007). For example, the histone variant *HTZ1* pattern correlates best with the nucleosome remodeler *SWR1,* which incorporates Htz1 into nucleosomes (Figs. 1D, S2B).

To our surprise we found that *rfa1-t11* correlated most strongly with *mre11Δ* in both the absence and presence of 20 mM HU (Fig. 1D). On 100 mM HU (Fig. S2B), the EMAP pattern of

rfa1-t11 correlated as well with *mec1-100*, an S-phase defective allele of Mec1 kinase that is particularly sensitive to HU (Paciotti et al., 2001). Indeed, at 100 mM HU these two alleles show an EMAP sensitivity that implicates the template switch pathway, whereas at 20 mM the patterns of sensitivity scored for *mre11Δ* and *rfa1-t11* resemble null alleles of replication fork components like *mrc1*Δ. We therefore examined in more detail the genetic relationship of *rfa1-t11, mec1-100* and deletion alleles of the MRX complex.

We created double mutants of *rfa1-t11* with deletions of *MRE11, RAD50* or *XRS2*, and tested them for epistasis on a range of DNA damaging agents. Confirming the EMAP we found that the sensitivity of *rfa1-t11* for growth on HU is completely epistatic with *mre11Δ, rad50Δ or xrs2Δ.* That is, single and double mutants had nearly identical survival rates on HU (Fig. 1E). The same is true for the triple mutant, *rfa1-t11 mre11Δ xrs2Δ,* on either HU or methylmethane sulfonate (MMS), an alkylating agent that also delays replication fork progression. On Zeocin, which induces single- and double-strand breaks, the two complexes again appeared to act on a common survival pathway, as the double mutants lacked additivity, although MRX loss of function alleles were significantly more sensitive than *rfa1-t11*. Nonetheless, these data confirmed that *rfa1-t11* likely acts through MRX and not on an alternative repair pathway at stalled forks and DSBs.

We next tested whether the *rfa1-t11* allele is epistatic or additive with mutations in Mec1, the checkpoint kinase, or the recombination protein Rad51. If *rfa1-t11's* main defect was an inability to load or modulate Rad51 on HU (Kantake et al., 2003) one would expect these two mutants to be epistatic. However, neither *rad51Δ* nor *mec1-100* was epistatic with the *rfa1-t11* allele (Fig. 1F), each showing strong synthetic lethality with *rfa1-t11* on HU. This suggests that

RPA works with MRX to maintain replication fork integrity on HU, defining a pathway that acts in parallel to checkpoint activation and to Rad51 (Fig. 1F). Consistently, *rad51Δ* was synergistically sensitive with *mre11Δ* and *mec1-100* on HU or MMS (Fig. 1F).

The replication fork is unable to resume after HU-induced arrest in the rfa1-t11 mutant

To examine how *rfa1-t11* affects replication fork integrity, we scored the resumption of replication after release from an acute fork arrest in 0.2 M HU. After 6h on HU, the recovery rate for *mec1-100* cells is < 10% of wild-type (wt) levels, while both the *mre11Δ* and *rfa1-t11* strains reduce recovery to about 20% of wt levels. Strikingly, the *rfa1-t11* mutant is again completely epistatic with the loss of Mre11 and is synergistically lethal with *mec1-100* (Fig. 2A). This places the *rfa1-t11* defect on the pathway through which MRX ensures fork restart on HU (Fig. 1D,E, S2).

To see if this reflects the loss of DNA polymerase α (polα) at forks arrested by 0.2M HU, we scored the presence of polα at forks that were arrested synchronously near early firing origins, using Chromatin immunoprecipitation (ChIP)(Cobb et al., 2003). In contrast to results in an isogenic wt background, we scored a striking loss of DNA polα at *ARS607* in the *rfa1-t11* mutant (Fig. 2B). This does not reflect an impaired checkpoint response, as there is no polα at the late firing origin *ARS501* (Fig. 2B), while in *mec1-100* cells impaired Rad53 activation allows late origin firing (Cobb et al., 2005).

To see if the resumption of DNA synthesis after HU arrest is compromised by *rfa1-t11*, we performed a DNA combing assay that measures fork progression by incorporation of a BrdU thymidine analogue after a transient exposure to 0.2 M HU and release into HU-free media.

Whereas wt forks resume elongation, the *rfa1-t11* mutant is strongly impaired in the resumption of DNA synthesis (white arrows, Fig. 2DE). Again, we note that the *rfa1-t11* defect is additive with *mec1-100.* Similar phenotypes have been observed in MRX deletion alleles, although not in mutants lacking Mre11 nuclease activity (Tittel-Elmer et al., 2009).

rfa1-t11 interferes with recruitment of MRX to stalled replication forks

Given the epistasis of *mre11Δ* with *rfa1-t11*, we examined whether the K45E mutation in RPA compromises the recruitment of MRX to stalled replication forks. We performed Rad50 ChIP after treatment with 0.2 M HU in wt and mutant strains. Indeed, by quantitative ChIP for Rad50-PK, we found that Rad50 recruitment to stalled forks at *ARS607* was compromised by the *rfa1-t11* mutation (Fig. 2F). To make sure that this was a general phenomenon and not unique to one site, we performed genome-wide ChIP of Rad50 on cells synchronously released from α-factor into 0.2 M HU. Figure 2G shows the pattern of Rad50 binding across a typical domain on Chr3, which includes several origins and non-origin binding sites. Whereas Rad50 binding at non-origin sites was not impaired in the *rfa1-t11* strain, its signal was strongly reduced at origins. We integrated this over all origins genome-wide (Fig. 2H), and found $\geq$ 50% reduction in MRX (Rad50) at origins on HU. Combining our data with observations of Tittel-Elmer *et al.,* 2012, we propose that Rfa1 recruits MRX to stalled replication forks, the failure of which allows replication fork collapse on HU soon after origin firing. This pathway of fork maintenance is independent of Rad53 activation (Fig. 2I).

MRX interacts with RPA through the N-OB fold of Rfa1

The epistasis and recruitment data on HU suggested that RPA might directly bind MRX. To detect this interaction and monitor its response to the *rfa1-t11* mutation, we co-

immunoprecipitated Rad50-PK from extracts of wt and *rfa1-t11* strains, probing for Rfa1 with an antibody that reacts equally with mutant and wt Rfa1 (Fig. 3A). We find that Rad50 can indeed co-precipitate Rfa1, while it binds rfa1-t11 less efficiently (Fig. 3B). The converse precipitation (i.e. by anti-Rfa1) confirmed that the MRX interaction was sensitive to the *rfa1-t11* mutation. The binding did not depend on DNA or RNA, since recovery was unchanged after treatment with Benzonase, which degrades nucleic acids (Figs. 3B, S3A). Pull-downs from cell extracts using antibody specific for Xrs2 recovered Rad50 and Rfa1, but failed to recover rfa1-t11 (Fig. 3B).

To determine the component of MRX that binds Rfa1, we repeated the Rad50-PK pulldown from extracts of *mre11Δ* or *xrs2Δ* strains. Rad50-PK precipitates a lower amount of Rfa1 in the absence of either Mre11 or Xrs2, suggesting either the existence of multiple contacts between Rfa1 and MRX, or a need for MRX complex integrity for the interaction (Fig. 3C). A double point mutation in Xrs2 (*xrs2-AA*) that disrupts Mre11 binding and/or the truncation (*xrs2-664)* of the Xrs2 C-terminus (Shima et al., 2005), compromised Rfa1 recovery to the same extent as *rfa1-t11* in *XRS2+* cells (Fig. S3B), suggesting a role for MRX conformation or complex integrity in Rfa1 interaction.

Finally, we examined the specificity of binding by comparing yeast two-hybrid (Y2H) interactions of Rfa1 with rfa1-t11. Intriguingly, both Mre11 and Xrs2 bound Rfa1 by Y2H, but only Xrs2 binding was *rfa1-t11* sensitive (Fig. S3CD). Y2H with Rad50 was not possible because the cloned fusions were lethal. Unfortunately, Y2H does not exclude that the endogenous MRX subunits form tertiary complexes with the bait during the assay, and thus from the Y2H and

pull-down results we concluded only that multiple contact sites exist between MRX and RPA, with a subset being sensitive to the *rfa1-t11* mutation.

To map the interactions more precisely, we used a scanning peptide microarray that consisted of 206 18-aa long peptides (overlapping by 9aa), covering all of MRX, except the coiled-coiled arms of Rad50. The peptides were spotted onto glass slides in triplicate, and were incubated with purified recombinant Rfa1 or *rfa1-t11* N-OB domains (Fig. 3D). Bound proteins were visualized through anti-Rfa1 staining and a secondary Alexa647-tagged antibody, whose fluorescence was quantified on a protein array analyzer (ImageJ plug-in, see Supplementary exp. procedures). The efficiency of binding of either Rfa1 or rfa1-t11 is plotted in Fig. 3E, and the full list of peptides and their associated intensities are in Table S2.

We scored several clusters of contacting peptides that were sensitive to the *rfa1-t11* mutation: namely, in the nuclease domain of Mre11, in the ATPase domain of Rad50, and two regions in Xrs2, one each in the N-terminal FHA domain and the C-terminal Mre11-binding domain (Fig. 3E). When mapped onto the 3D structure of Mre11-Rad50 (Seifert et al., 2015), the peptides cluster in two surface areas: the dsDNA binding cleft of the Rad50 dimer, and a surface patch on the lateral side of the Mre11 phosphodiesterase domain (Fig. 3F). While peptides from Xrs2 also showed differential interaction, two of these map to binding sites for other proteins, and they do not cluster as do those in Mre11 or Rad50. Microscale thermophoresis (MST) showed that the Rad50 peptide 17 had the highest affinity for Rfa1-N (Fig. 3G). The other peptides tested showed weaker binding. This does not rule out that they contribute to a binding site, but suggests that the ATPase-domain of Rad50 contains a key interaction site, which is indeed sensitive to the K45E mutation.

rfa1-t11 impairs Mec1-dependent checkpoint activation at DSBs

Since *rfa1-t11* had previously been shown to be important to recruit Ddc2 (ATRIP) and Mec1 (ATR) to a DSB (Dubrana et al., 2007; Zou and Elledge, 2003) we next interrogated its genetic relationship with *mec1-100* on Zeocin, which induces both single- and double-strand breaks. While *rfa1-t11* is sensitive to Zeocin, *mec1-100* has but a mild slow-growth phenotype (Fig. 4A). Surprisingly, and in contrast to growth on HU or MMS where the combination of *rfa1-t11* and *mec1-100* was synthetically lethal, the combination of *rfa1-t11* and *mec1-100* was epistatic on Zeocin. MRX both helps to recruit the DNA damage checkpoint kinase Tel1 (ATM) to DSBs (Nakada et al., 2003a; Nakada et al., 2003b), and promotes resection to allow Ddc2-Mec1 activation.

To check the epistatic relationship of Rfa1 and Mre11 on Zeocin, we scored the effects of *rfa1-t11, mre11Δ, tel1Δ*, and their pairwise combinations on Rad53 phosphorylation. We found that *rfa1-t11* and *mre11Δ* mutations compromised checkpoint activation by Zeocin to a similar degree (Fig. 4B), yet in the case of *rfa1-t11*, the impaired checkpoint response was strongly additive with *tel1Δ*; i.e. the *tel1Δ rfa1-t11* completely failed to activate the DNA damage checkpoint (Fig. 4B). This suggests that the *rfa1-t11* defect in checkpoint at DSBs arises from the loss of Mec1 (ATR) activity. Indeed, by ChIP *rfa1-t11* and *rad50Δ* were shown to reduce the accumulation of phosphorylated H2A (γH2A, a Mec1 target), at an HO-induced DSB (Fig. 4C). We conclude that *rfa1-t11* compromises the Mec1 checkpoint response at DNA breaks (i.e. on Zeocin), but does not impair Mec1 activation at stalled forks. This difference likely stems from the redundancy of co-activators at stalled forks, namely 9-1-1, Dbp11, Mrc1, Sgs1 and RPA (Hustedt et al., 2013). We note that although DSB activation of checkpoint kinases was

compromised by *rfa1-t11*, both the efficiency of HO endonuclease cleavage and resection rates were at wt levels (Fig. 4DE).

rfa1-t11 reduces recruitment of MRX to DSBs and reduces repair efficiency

To see whether RPA is implicated in the recruitment or stabilization of MRX at DSBs, possibly by binding either a short overhang or an internal ss stretch, we measured the recruitment Rad50-PK to a HO endonuclease-induced DSB at *MAT* by ChIP. Consistent with previously published results, MRX binding is strongest at early time points and close to the cut site (compare 0.6 vs 1.6 kb probes). This interaction is reduced (although not entirely eliminated) in the *rfa1-t11* mutant (Fig. 5A). Consistently, Mre11-YFP focus formation was reduced by roughly 50% in response to Zeocin in the *rfa1-t11* mutant (Fig. 5B). One further function attributed to MRX at DSBs is the recruitment of cohesin (Unal et al., 2004; Unal et al., 2007). We therefore tested whether *rfa1-t11,* like *rad50*Δ, fails to recruit cohesin to an HO-induced DSB. ChIP for cohesin subunit Scc1-HA (Mcd1) at a DSB confirmed that both reduce cohesin recruitment similarly at 120 min after HO induction (Fig. 5C).

In contrast to the observation that *rfa1-t11* decreases MRX levels at DSBs, it was recently published that the loss of Sae2 leads to more MRX at DSBs (Chen et al., 2015; Gobbini et al., 2015). We therefore tested whether *sae2*Δ would compensate for the reduced RPA-MRX binding in the *rfa1-t11* mutant. Indeed, growth defects of *rfa1-t11* on Zeocin, HU, MMS and the topoisomerase I inhibitor camptothecin, were partially rescued by the elimination of Sae2 (Fig. S3E). Again, this supports the model that *rfa1-t11* confers sensitivity to DNA damage due to impaired MRX recruitment.

To see if this affects DSB repair by a pathway other than HR, we tested the impact of the *rfa1-t11* mutation on repair by end-joining of two incompatible DSBs that flank a *URA3* reporter gene (Ma et al., 2003; Matsuzaki et al., 2012). After cleavage and repair, the survivors are either *URA*- (indicating repair by microhomology mediated repair of non-complementary DSB ends following resection), or *URA+* (precise end-ligation). Like mutations in the MRX complex, *rfa1-t11* reduced the recovery of both *URA*- and *URA+* colonies (Fig. 5D). Importantly, the *xrs2Δ* mutation is epistatic with *rfa1-t11* in this assay (Iwasaki et al., 2016), consistent with drop assays on Zeocin that place MRX and Rfa1 on the same repair pathway. Given that *rfa1-t11* does not block resection, we suggest that RPA acts by recruiting or stabilizing MRX at breaks, allowing it to hold the two break ends together for either precise or imprecise end-joining.

RFA1 OB-fold integrity is necessary to allow MRX to hold the ends of a DSB together

We next tested whether *rfa1-t11* directly interferes with the end-tethering activity of MRX by scoring the separation of ends by tagged with different fluorescent protein fusions on either side of an inducible DSB (Kaye et al., 2004; Lobachev et al., 2004). As expected, following cleavage by a galactose-inducible I-SceI endonuclease, the loss of MRX integrity provoked a significant increase in DSB end separation in cells arrested at G2/M by the DNA damage checkpoint (Fig. 6A; see also Kaye et al., 2004; Lobachev et al., 2004). Importantly, the level of end separation scored for *mre11Δ* and *rad50Δ* mutants, was the same for *rfa1-t11* (Fig. 6A).

The fact that *rfa1-t11* compromised cohesin loading (Fig. 5C), led us to test whether this mutation interferes with the tight association of sister chromatids, which we could score in a strain bearing a *lacO* array adjacent to the HO-incuded break at *MATα* (Fig. 6B). Sister cohesion at DSBs is commonly ascribed to cohesin, but on the basis of its architecture and dimensions,

MRX should also be able to hold sister chromatids together (Hopfner et al., 2002). To test a potential role for MRX in sister-sister pairing at breaks, we used multiple DSB imaging approaches. First, super-resolution structured illumination microscopy (SIM) was used to analyze small changes in the area occupied by the paired *lacO* arrays adjacent to a break, in late S/G2 phase cells. Second, we performed high speed time-lapse imaging of the arrays to measure the kinetics of separation following break induction, in unarrested S-phase cells. Finally, we examined the maintenance of sister-sister juxtaposition after efficient DSB induction in cells that are arrested by microtubule depolymerization and fixed, comparing *rfa1-t11* with mutants in cohesin and MRX.

We first confirmed that we can resolve two sister chromatids with 3D SIM imaging of the cleaved *MATα* locus (Fig. 6BC). Following projection of the 3D image stack to a 2D plane for a large number of late S-phase cells, we found that the area and shape of the fluorescent *lacO* signal are significantly larger in the *rfa1*-t11 mutant, even though the sisters only fully separated in $<$1% of cells (Fig. 6CD). We next confirmed the validity of this spot-size assay by using a strain in which the essential cohesin subunit Scc1 (Mcd1) was cleaved by a galactose-induced TEV protease (Fig. 6D). The efficiency of Scc1 cleavage was documented by Western blot (Fig. S4AB). In S-phase cells we scored a robust increase in the area occupied by the cut-proximal *lacO* focus after Scc1 cleavage, presumably reflecting compromised pairing of sister chromatids (arrow, Fig. 6D, S4C). We applied the same analysis to the strain bearing a HO-mediated DSB at the *MATα* locus adjacent to a *lacO* array (Fig. 6B). In wt cells there is a slight increase in array area as cells progress from G1 to S phase; at 120 min after HO induction, there is again a slight increase in locus size (Fig. 6D). In the *rfa1-t11* or *rad50Δ* strains, however, the

size of the *lacO* signal stemming from the two sisters, increased more significantly than was detected upon Scc1 cleavage (Fig. 6D, 0.9 vs 0.6 µm2).

Given that chromatin loci show continual movement in living cells, and that fixation can introduce artefacts, we examined the behavior of the *lacO* arrays on the two tagged sisters using a high-speed/high-resolution imaging assay with and without cut induction (Fig. 7). In the strains used in Fig. 6B, we acquired z-stacks on a spinning-disk confocal microscope (8x 0.2 nm z-stacks, 10 ms exposure) continuously over 1 min, yielding 750 stacks per movie at a 3D spatial resolution of ~256 nm. The movies were projected stack by stack on to a 2D plane for analysis by the ImageJ (Fiji) plugin Trackmate (Supplemental Exp. Procedures), and we quantified the % of frames in which two spots can be resolved. Again we used the TEV-cleavable Scc1 strain to confirm that we can monitor a loss of sister chromatid cohesion at a tagged *ARS607* (Fig. S4DE). Spot separation was very low in a normal wt S phase (~2% of frames separated), while after 1h TEV induction, separation increased to ~11% (Fig. S4E).

Next we induced HO-mediated cleavage at *MATα* (Fig. 7A) and monitored sister chromatid dynamics in wt, *rad50Δ* or *rfa1-t11* cells. After 2h of HO induction in wt S-phase cells, 8% of the frames showed resolution of the two sisters into two spots, while in either *rad50Δ* or *rfa1-t11* strains, 16 to 19% of the frames had separated sisters (Fig. 7B). We ruled out that this is an artefact of galactose addition by expressing HO in a strain that is resistant to cleavage, $mata^{inc}$. In conclusion, sister chromatid juxtaposition at a DSB is compromised by loss of MRX or its recruitment through RPA.

To see if this reflects compromised bridging through MRX itself or a failure to recruit and load cohesin at the DSB (Fig. 5C; Unal *et al.,* 2007), we tested the effects of destabilizing Scc1 (Mcd1) at the base of the cohesin ring (Fig. 7A). Specifically, we scored sister *lacO* foci pairing at the induced cut at *MATα* in a ts allele of Scc1 called *mcd1-1* (Uhlmann et al., 2000). Previous studies showed that a 1h incubation at the non-permissive temperature (37°C), was sufficient to inactivate cohesin. Our time-lapse imaging showed that without DSB induction, S-phase *mcd1-1* cells have separated *lacO* foci in ~25% of frames at 37°C (Fig. 7C). Remarkably, after DSB induction and cohesin cleavage (1h at 37°C), spot separation was actually reduced to 5%, suggesting that the induction of the break stabilizes sister-sister pairing. Importantly, this effect was reversed by combining the ts *mcd1-1* mutant with *rfa1-t11* (Fig. 7C). This argues that MRX holds sister chromatids together at a DSB, even in the absence of functional cohesin. We note that this result is in contrast to a previous report where a DSB was not sufficient to keep sisters together (Unal et al., 2007), although in that case an unusual construction with two DSBs was used, and separation was induced and monitored after 4 h of Nocodazole arrest. Under those conditions cohesin seemed to contribute to sister cohesion.

To rule out kinetic limitations of our timelapse assay, which scores unfixed cells immediately after cleavage, we tested an experimental setup much like that used in Unal *et al.,* 2007. The cells were grown to log phase and Nocodazole was added at the same time as either glucose (no HO cut) or galactose (induction of HO). After 1h, cells were shifted to 37°C to inactivate cohesin, and cells were fixed and imaged. G2/M cells were scored for LacI-GFP spot separation (Fig. 7D). Remarkably we found that whereas loss of the cohesin ring (*mcd1-1* at 37°C) allowed sisters to separate at an uncut locus, sister pairing was restored in a manner dependent on

Rad50 (MRX) and a functional Rfa1 N-terminal OB fold after cut induction (Fig. 7D-F). This argues that upon DSB induction, the recruitment of MRX by Rfa1 is necessary and sufficient to hold both DSB ends and two broken sister chromatids together, as this can be achieved in the absence of intact cohesin (Fig. 7F).

Discussion

Since their discovery and description in the 1990's it has long been debated what role the family of SMC protein complexes play in the tethering of broken DNA ends or in the maintenance of sister chromatid pairing (Huang and Kolodner, 2005; Nasmyth and Haering, 2005; Uhlmann, 2016). MRX is closely related to cohesin, condensin and the SMC5/6 complex, given the long coiled-coil domains of Rad50 and the head group dimerization function of Mre11 and Xrs2 (Stracker and Petrini, 2011). Indeed, we document here an "SMC-like" function for the MRX complex at DSBs, where it appears not only to hold ends together, but to contribute to the pairing of broken sisters. In this function the recruitment of MRX is compromised by a mutation in the N-terminal domain of Rfa1. This helps answer the long-standing question as to how MRX is targeted to sites of damage. While MRX interaction with RPA may not be entirely compromised in the *rfa1-t11* mutant, the epistatic relationship of these mutations on both HU and Zeocin argues that the interaction is important in the context of DNA damage or replication fork arrest.

rfa1-t11 and MRX mutations work epistatically to compromise fork integrity under stress

By EMAP analysis against a panel of 1311 knock-out alleles, we found that the sensitivity of *rfa1-t11* to HU parallels that of *mre11*Δ (Fig. 1). In all fork-stalling and recovery assays

performed, *rfa1-t11* acted epistatically with MRX mutations. Consistently, MRX recruitment to HU-stalled forks is compromised by the *rfa1-t11* mutation, yet *rfa1-t11* does not impair activation of the replication checkpoint on HU. Rad53 is efficiently phosphorylated in both the *mre11*Δ and *rfa1-t11* strains on HU (Kanoh et al., 2006). As expected, *rfa1-t11* defects are additive with *mec1-100,* an S-phase specific allele of the ATR kinase, Mec1, which fails to activate Rad53 in response to replication stress (Cobb et al., 2005; Hustedt et al., 2015). At stalled forks, MRX is thought both to process fold-back structures, preventing ligation or over-resection, and to tether replicated sisters together, prior to the loading of cohesin (Tittel-Elmer et al., 2012)**.**

The MRX complex has a structural role at DSBs

We also document a clear but unanticipated role for Rfa1 in the recruitment and stability of MRX at DSBs (Figs. 5-7). MRX tethering by RPA at breaks in late S phase contributes both to end-to-end tethering and the juxtaposition of broken sisters (late S/G2). On Zeocin, the *rfa1-t11* mutation compromises Rad53 activation in a manner independent of Tel1 (ATM), which likely reflects a role for the Rfa1 N-terminal OB-fold in the recruitment of Rad9 (53BP1). Rad9 stimulates Mec1-dependent phosphorylation of Rad53 at breaks (Sweeney et al., 2005). Again, we have tested the effects of *rfa1-t11* in a range of yeast backgrounds, generating the mutant allele by *de novo* mutagenesis. In all cases *rfa1-t11* was epistatic to *mre11Δ*.

A previous study (Unal et al., 2007) examined the role of MRX in sister chromatid cohesion, and documented a role for MRX in the recruitment of cohesin (Unal et al., 2007). We confirmed that MRX recruits cohesin, but we found that it is MRX, and not cohesin, that holds sisters together at breaks at early time points. Our experiments differ from theirs in two significant ways: first,

they induced two sets of DSBs near each other, while we induced only one. Second, Unal *et al.* first treated cells with the microtubule depolymerizing drug Nocodazole for 4 h before inducing the DSB for a further 2 h. This extended arrest in G2/M may alter the behavior of the break.

It is unclear how MRX contributes to cohesin loading, since the two proteins do not interact (Tittel-Elmer et al., 2012). It may simply be that MRX holds sisters together to allow cohesin loading. In any case, it appears that through its interaction with Rfa1, MRX serves an additional role at DSBs by stabilizing both end-to-end and sister-sister contacts.

A recent report studied the role of the Rad50 zinc hook in DSB repair by monitoring sister chromatid exchange in mitosis. They found that strains with mutations in the zinc hook domain that partially impair hook dimerization without blocking complex assembly, have milder effects on sister chromatin exchange than full *RAD50* deletions (Hohl et al., 2015). We propose that these hook mutations reduce, but do not ablate, Rad50 dimerization. At a DSB multiple MRX molecules bind and even with a weakened Rad50 hook, their combined effect may be sufficient to hold both ends and sisters together (Figs. 6,7). Cohesin may provide further structural support later in repair.

Rfa1 interaction sites on MRX are relevant to biological function and human disease

The validated interaction sites between Rfa1 and MRX cluster in two major sites. One is located in the DNA binding cleft of the Rad50 dimer. In the presence of ATP, Rad50 primarily binds dsDNA and duplexes with extended 3' overhangs (Seifert et al., 2015). Thus, the location of the interacting peptides would be consistent with a side-by-side binding of Rad50 and RPA at ssDNA/dsDNA junctions. The second cluster of interacting peptides maps to a surface on the N-

terminal phosphodiesterase domain of Mre11 (peptides 9 – 12, Table S3), which was recently shown to be mutated in Mre11 hypomorphic alleles that suppress the damage sensitivity of *sae2Δ* (Seifert et al., 2015). This mutation allows MRX to be more easily removed from ssDNA during the later stages of HR (Chen et al., 2015).

In addition, the Mre11 peptide #25 (aa 217 to 234), which binds Rfa1 in a *rfa1-t11* sensitive manner *in vitro*, contains a site that is mutated in patients suffering from ataxia-telangiectasia-like disease (ATLD; Mre11 mutations W210C and W243R) (Fernet et al., 2005; Regal et al., 2013; Schiller et al., 2012). Very close to this interaction site is the *mre11-58* mutation (H213Y), which confers a rad50-S-like phenotype (Usui et al., 1998), affecting Mre11's nuclease activity and/or its interaction to Nbs1/Xrs2 (Schiller et al., 2012). The fact that this domain interacts with Rfa1 in an *rfa1-t11* sensitive manner suggests that a loss of Rfa1 binding may also contribute to the ATLD phenotypes. We note that some interactions sites may require switching between open and closed conformational states of MRX (Lim et al., 2011; Mockel et al., 2012) and that some of Rfa1-MRX interactions are insensitive to the *rfa1-t11* mutation. In the case of Mre11 peptides #37-39, interaction was enhanced with the mutant Rfa1 domain. Intriguingly, this conserved Mre11 region is deleted in some ATLD patients (Δ340-366) who are predisposed to pulmonary adenocarcinoma (Regal et al., 2013).

High speed and super resolution imaging allow new insights into chromatin biology

We have been able analyze sister chromatid pairing with super resolution microscopy of short fluorescent tags either on the two sisters or both sides of a DSB. While the resolution achieved here (250 nm and 80 ms 3D stack imaging) is sufficient to document sister separation, the imaging method can be improved to provide even more information about the forces that hold

sisters together. Extending these experiments to include other SMC proteins such as condensin or the SMC5/6 complex, will surely provide a fuller understanding of long-range chromatin interactions in living cells.

Experimental procedures

Yeast growth conditions, plasmids, repair assays and ChIP

All strains used were derived from W303-1A or JKM179 (see Table S1). EMAP, drop assays and DNA combing methods are described in Supplemental exp. procedures. Cohesin experiments used Nocodazole at 15 µg/ml with the yeast culture adjusted to 1% DMSO before Nocodazole addition. Imprecise and precise NHEJ assay were as in Matsuzaki et al., 2012. ChIP experiments were performed as described in Cobb et al., 2003. For ChIP-chip and associated bioinformatics analysis see Tittel-Elmer et al., 2012.

Protein purification, structure studies, peptide arrays and microscale thermophoresis

Details are presented in Supplemental exp. Pprocedures. The scanning peptide array covered all of MRX except the coiled-coil domains of Rad50, with 18-aa long peptides with 9-aa overlap spotted onto a glass slide by JPT Peptide Technologies GmbH.

Microscopy and error calculation

Details for live and fixed fluorescent imaging and quantitative analysis including spot volume and spot separation in time lapse movies are described in Supplemental exp. procedures. Structured illumination imaging used a Zeiss Elyra S.1 microscope with an Andor iXon 885 EMCCD camera.

Error bars on graphs represent the standard error of the mean unless otherwise stated. Categorical data such as the 1 vs 2 spot cohesin assay was tested for significance using a two-tailed Fisher exact test (Graph Pad), computing exact P values using the method of summing small P values. The large spot separation movie dataset was tested for significance using a Chi-square with Yates correction test (Graph Pad) against the relevant strain genotype uncut. Continuous data such as LacI-GFP spot size was shown to be normally distributed and then tested for differences using a two-tailed Student's t-test (Graph Pad). Significance cut off was $P < 0.05$. All P values are in Table S4.

Accession numbers

The accession number of the rfa1-t11 N-OB crystal structure is PDB: 5M1X

Author contributions

A.S., K.S. and S.M.G planned experiments, analyzed data and wrote the manuscript. A.S. and A.M.H. performed most experiments, N.H. carried out the EMAP, J.P. did Rad50 ChIP-chip, I.D. did MST, purified Rfa1 and determined rfa1-t11 structure guided by H.G., M.S. did the NHEJ assay, J.E. wrote scripts for image analysis, K.S. created strains, and K-P.H. modeled the Rad50-Mre11 structure and peptide position. P.P. supervised DNA combing and ChIP-chip data.

Acknowledgments

We thank J. Bianco and the Pasero lab for assistance, M. Stadler for statistical analysis, L. Gelman and S. Bourke for imaging help, C. Soustelle and A. Nicolas for the *rfa1-t11* plasmid, M. Kawai for technical assistance, J. Cobb for advice, K. Lobachev, K. Bloom, D. Koshland and M. Resnick for strains, and J. Petrini for the Mre11 antibody. We thank V. Dion, U. Rass and Gasser

lab members for proofreading. The Gasser laboratory thanks the SNSF, HFSP, EMBO, and the Novartis Research Foundation for support.

References

Ball, H.L., Ehrhardt, M.R., Mordes, D.A., Glick, G.G., Chazin, W.J., and Cortez, D. (2007). Function of a conserved checkpoint recruitment domain in ATRIP proteins. Mol Cell Biol *27*, 3367-3377.

Binz, S.K., and Wold, M.S. (2008). Regulatory functions of the N-terminal domain of the 70-kDa subunit of replication protein A (RPA). J Biol Chem *283*, 21559-21570.

Bjergbaek, L., Cobb, J.A., Tsai-Pflugfelder, M., and Gasser, S.M. (2005). Mechanistically distinct roles for Sgs1p in checkpoint activation and replication fork maintenance. Embo J *24*, 405-417.

Bochkareva, E., Kaustov, L., Ayed, A., Yi, G.S., Lu, Y., Pineda-Lucena, A., Liao, J.C., Okorokov, A.L., Milner, J., Arrowsmith, C.H.*, et al.* (2005). Single-stranded DNA mimicry in the p53 transactivation domain interaction with replication protein A. Proc Natl Acad Sci U S A *102*, 15412-15417.

Chen, H., Donnianni, R.A., Handa, N., Deng, S.K., Oh, J., Timashev, L.A., Kowalczykowski, S.C., and Symington, L.S. (2015). Sae2 promotes DNA damage resistance by removing the Mre11-Rad50-Xrs2 complex from DNA and attenuating Rad53 signaling. Proc Natl Acad Sci U S A *112*, 1880-1887.

Ciccia, A., and Elledge, S.J. (2010). The DNA damage response: making it safe to play with knives. Mol Cell *40*, 179-204.

Cobb, J.A., Bjergbaek, L., Shimada, K., Frei, C., and Gasser, S.M. (2003). DNA polymerase stabilization at stalled replication forks requires Mec1 and the RecQ helicase Sgs1. Embo J *22*, 4325-4336.

Cobb, J.A., Schleker, T., Rojas, V., Bjergbaek, L., Tercero, J.A., and Gasser, S.M. (2005). Replisome instability, fork collapse, and gross chromosomal rearrangements arise synergistically from Mec1 kinase and RecQ helicase mutations. Genes Dev *19*, 3055-3069.

de Jager, M., Dronkert, M.L., Modesti, M., Beerens, C.E., Kanaar, R., and van Gent, D.C. (2001a). DNA-binding and strand-annealing activities of human Mre11: implications for its roles in DNA DSB repair pathways. Nucleic Acids Res *29*, 1317-1325.

de Jager, M., van Noort. J., van Gent, D., Dekker, C., Kanaar, R., Wyman, C., (2001b). Human Rad50/Mre11 Is a Flexible Complex that Can Tether DNA Ends. Mol Cell *8,* 1129-1135.

Dubrana, K., van Attikum, H., Hediger, F., and Gasser, S.M. (2007). The processing of double-strand breaks and binding of single-strand-binding proteins RPA and Rad51 modulate the formation of ATR-kinase foci in yeast. J Cell Sci *120*, 4209-4220.

Dutta, A., Ruppert, J.M., Aster, J.C., and Winchester, E. (1993). Inhibition of DNA replication factor RPA by p53. Nature *365*, 79-82.

Fernet, M., Gribaa, M., Salih, M.A., Seidahmed, M.Z., Hall, J., and Koenig, M. (2005). Identification and functional consequences of a novel MRE11 mutation affecting 10 Saudi Arabian patients with the ataxia telangiectasia-like disorder. Hum Mol Genet *14*, 307-318.

Flynn, R.L., and Zou, L. (2010). Oligonucleotide/oligosaccharide-binding fold proteins: a growing family of genome guardians. Crit Rev Biochem Mol Biol *45*, 266-275.

Garcia, V., Phelps, S.E., Gray, S., and Neale, M.J. (2011). Bidirectional resection of DNA double-strand breaks by Mre11 and Exo1. Nature *479*, 241-244.

Gobbini, E., Villa, M., Gnugnoli, M., Menin, L., Clerici, M., and Longhese, M.P. (2015). Sae2 Function at DNA DSBs Is Bypassed by Dampening Tel1 or Rad53 Activity. PLoS Genet *11*, e1005685.

Gonzalez-Barrera, S., Cortes-Ledesma, F., Wellinger, R.E., and Aguilera, A. (2003). Equal sister chromatid exchange is a major mechanism of double-strand break repair in yeast. Mol Cell *11*, 1661-1671.

Harrison, J.C., and Haber, J.E. (2006). Surviving the breakup: the DNA damage checkpoint. Annu Rev Genet *40*, 209-235.

Hartsuiker, E., Vaessen, E., Carr, A.M., and Kohli, J. (2001). Fission yeast Rad50 stimulates sister chromatid recombination and links cohesion with repair. Embo J *20*, 6660-6671.

Hegnauer, A.M., Hustedt, N., Shimada, K., Pike, B.L., Vogel, M., Amsler, P., Rubin, S.M., van Leeuwen, F., Guenole, A., van Attikum, H.*, et al.* (2012). An N-terminal acidic region of Sgs1 interacts with Rpa70 and recruits Rad53 kinase to stalled forks. Embo J *31*, 3768-3783.

Heidinger-Pauli, J.M., Unal, E., Guacci, V., and Koshland, D. (2008). The kleisin subunit of cohesin dictates damage-induced cohesion. Mol Cell *31*, 47-56.

Hirano, T. (2006). At the heart of the chromosome: SMC proteins in action. Nat Rev Mol Cell Biol *7*, 311-322.

Hohl, M., Kochańczyk, T., Tous, C., Aguilera A., Krężel, A., Petrini, J.H. (2015). Interdependence of the rad50 hook and globular domain functions. Mol Cell *57*, 479-491.

Hopfner, K.P., Craig, L., Moncalian, G., Zinkel, R.A., Usui, T., Owen, B.A., Karcher, A., Henderson, B., Bodmer, J.L., McMurray, C.T.*, et al.* (2002). The Rad50 zinc-hook is a structure joining Mre11 complexes in DNA recombination and repair. Nature *418*, 562-566.

Huang, M.E., and Kolodner, R.D. (2005). A biological network in Saccharomyces cerevisiae prevents the deleterious effects of endogenous oxidative DNA damage. Mol Cell *17*, 709-720.

Hustedt, N., Gasser, S.M., and Shimada, K. (2013). Replication checkpoint: tuning and coordination of replication forks in s phase. Genes *4*, 388-434.

Hustedt, N., Seeber, A., Sack, R., Tsai-Pflugfelder, M., Bhullar, B., Vlaming, H., van Leeuwen, F., Guenole, A., van Attikum, H., Srivas, R.*, et al.* (2015). Yeast PP4 interacts with ATR homolog Ddc2-Mec1 and regulates checkpoint signaling. Mol Cell *57*, 273-289.

Iwasaki, D., Hayashihara, K., Shima, H., Higashide, M., Terasawa, M., Gasser, S.M., and Shinohara, M. (2016). The MRX Complex Ensures NHEJ Fidelity through Multiple Pathways Including Xrs2-FHA-Dependent Tel1 Activation. PLoS Genet *12*, e1005942.

Kanoh, Y., Tamai, K., and Shirahige, K. (2006). Different requirements for the association of ATR-ATRIP and 9-1-1 to the stalled replication forks. Gene *377*, 88-95.

Kantake, N., Sugiyama, T., Kolodner, R.D., and Kowalczykowski, S.C. (2003). The recombination-deficient mutant RPA (rfa1-t11) is displaced slowly from single-stranded DNA by Rad51 protein. J Biol Chem *278*, 23410-23417.

Kaye, J.A., Melo, J.A., Cheung, S.K., Vaze, M.B., Haber, J.E., and Toczyski, D.P. (2004). DNA breaks promote genomic instability by impeding proper chromosome segregation. Curr Biol *14*, 2096-2106.

Lafrance-Vanasse, J., Williams, G.J., and Tainer, J.A. (2015). Envisioning the dynamics and flexibility of Mre11-Rad50-Nbs1 complex to decipher its roles in DNA replication and repair. Progress in biophys mol biol *117*, 182-193.

Lengsfeld, B.M., Rattray, A.J., Bhaskara, V., Ghirlando, R., and Paull, T.T. (2007). Sae2 is an endonuclease that processes hairpin DNA cooperatively with the Mre11/Rad50/Xrs2 complex. Mol Cell *28*, 638-651.

Lim, H.S., Kim, J.S., Park, Y.B., Gwon, G.H., and Cho, Y. (2011). Crystal structure of the Mre11-Rad50-ATPγS complex: understanding the interplay between Mre11 and Rad50. Genes Dev *25*, 1091-1104.

Lisby, M., Barlow, J.H., Burgess, R.C., and Rothstein, R. (2004). Choreography of the DNA damage response: spatiotemporal relationships among checkpoint and repair proteins. Cell *118*, 699-713.

Lobachev, K., Vitriol, E., Stemple, J., Resnick, M.A., and Bloom, K. (2004). Chromosome fragmentation after induction of a double-strand break is an active process prevented by the RMX repair complex. Curr Biol *14*, 2107-2112.

Ma, J.L., Kim, E.M., Haber, J.E., and Lee, S.E. (2003). Yeast Mre11 and Rad1 proteins define a Ku-independent mechanism to repair double-strand breaks lacking overlapping end sequences. Mol Cell Biol *23*, 8820-8828.

Matsuzaki, K., Terasawa, M., Iwasaki, D., Higashide, M., and Shinohara, M. (2012). Cyclin-dependent kinase-dependent phosphorylation of Lif1 and Sae2 controls imprecise nonhomologous end joining accompanied by double-strand break resection. Genes Cells *17*, 473-493.

Mimitou, E.P., and Symington, L.S. (2008). Sae2, Exo1 and Sgs1 collaborate in DNA double-strand break processing. Nature *455*, 770-774.

Mockel, C., Lammens, K., Schele, A., and Hopfner, K.P. (2012). ATP driven structural changes of the bacterial Mre11:Rad50 catalytic head complex. Nucleic Acids Res *40*, 914-927.

Morrison, A.J., Kim, J.A., Person, M.D., Highland, J., Xiao, J., Wehr, T.S., Hensley, S., Bao, Y., Shen, J., Collins, S.R*., et al.* (2007). Mec1/Tel1 phosphorylation of the INO80 chromatin remodeling complex influences DNA damage checkpoint responses. Cell *130*, 499-511.

Nakada, D., Matsumoto, K., and Sugimoto, K. (2003a). ATM-related Tel1 associates with double-strand breaks through an Xrs2-dependent mechanism. Genes Dev *17*, 1957-1962.

Nakada, D., Shimomura, T., Matsumoto, K., and Sugimoto, K. (2003b). The ATM-related Tel1 protein of *S. cerevisiae* controls a checkpoint response following phleomycin treatment. Nucleic Acids Res *31*, 1715-1724.

Nasmyth, K., and Haering, C.H. (2005). The structure and function of SMC and kleisin complexes. Annu Rev Biochem *74*, 595-648.

Paciotti, V., Clerici, M., Lucchini, G., and Longhese, M.P. (2000). The checkpoint protein Ddc2, functionally related to S. pombe Rad26, interacts with Mec1 and is regulated by Mec1-dependent phosphorylation in budding yeast. Genes Dev *14*, 2046-2059.

Paciotti, V., Clerici, M., Scotti, M., Lucchini, G., and Longhese, M.P. (2001). Characterization of mec1 kinase-deficient mutants and of new hypomorphic mec1 alleles impairing subsets of the DNA damage response pathway. Mol Cell Biol *21*, 3913-3925.

Petermann, E., and Helleday, T. (2010). Pathways of mammalian replication fork restart. Nat Rev Mol Cell Biol *11*, 683-687.

Regal, J.A., Festerling, T.A., Buis, J.M., and Ferguson, D.O. (2013). Disease-associated MRE11 mutants impact ATM/ATR DNA damage signaling by distinct mechanisms. Hum Mol Genet *22*, 5146-5159.

Rouse, J., and Jackson, S.P. (2002). Lcd1p recruits Mec1p to DNA lesions in vitro and in vivo. Mol Cell *9*, 857-869.

San Filippo, J., Sung, P., and Klein, H. (2008). Mechanism of eukaryotic homologous recombination. Annu Rev Biochem *77*, 229-257.

Schiller, C.B., Lammens, K., Guerini, I., Coordes, B., Feldmann, H., Schlauderer, F., Möckel, C., Schele, A., Strässer, K., Jackson, S.P*., et al.* (2012). Structure of Mre11–Nbs1 complex yields insights into

ataxia-telangiectasia–like disease mutations and DNA damage signaling. Nat Struct Mol Biol *19*, 693-700.

Seifert, F.U., Lammens, K., and Hopfner, K.P. (2015). Structure of the catalytic domain of Mre11 from *Chaetomium thermophilum*. Acta crystallographica Section F, Struct biol comm *71*, 752-757.

Shima, H., Suzuki, M., and Shinohara, M. (2005). Isolation and characterization of novel *xrs2* mutations in *S. cerevisiae.* Genetics *170*, 71-85.

Stracker, T.H., and Petrini, J.H. (2011). The MRE11 complex: starting from the ends. Nat Rev Mol Cell Biol *12*, 90-103.

Strom, L., Karlsson, C., Lindroos, H.B., Wedahl, S., Katou, Y., Shirahige, K., and Sjogren, C. (2007). Postreplicative formation of cohesion is required for repair and induced by a single DNA break. Science *317*, 242-245.

Strom, L., and Sjogren, C. (2007). Chromosome segregation and double-strand break repair - a complex connection. Curr Opin Cell Biol *19*, 344-349.

Sweeney, F.D., Yang, F., Chi, A., Shabanowitz, J., Hunt, D.F., and Durocher, D. (2005). S. cerevisiae Rad9 acts as a Mec1 adaptor to allow Rad53 activation. Curr Biol *15*, 1364-1375.

Tittel-Elmer, M., Alabert, C., Pasero, P., and Cobb, J.A. (2009). The MRX complex stabilizes the replisome independently of the S phase checkpoint during replication stress. Embo j *28*, 1142-1156.

Tittel-Elmer, M., Lengronne, A., Davidson, Marta B., Bacal, J., François, P., Hohl, M., Petrini, John H.J., Pasero, P., and Cobb, J.A. (2012). Cohesin Association to Replication Sites Depends on Rad50 and Promotes Fork Restart. Mol Cell *48*, 98-108.

Toledo, L.I., Altmeyer, M., Rask, M.B., Lukas, C., Larsen, D.H., Povlsen, L.K., Bekker-Jensen, S., Mailand, N., Bartek, J., and Lukas, J. (2013). ATR prohibits replication catastrophe by preventing global exhaustion of RPA. Cell *155*, 1088-1103.

Uhlmann, F. (2016). SMC complexes: from DNA to chromosomes. Nat Rev Mol Cell Biol *17*, 399-412.

Uhlmann, F., Lottspeich, F., and Nasmyth, K. (1999). Sister-chromatid separation at anaphase onset is promoted by cleavage of the cohesin subunit Scc1. Nature *400*, 37-42.

Uhlmann, F., Wernic, D., Poupart, M.A., Koonin, E.V., and Nasmyth, K. (2000). Cleavage of cohesin by the CD clan protease separin triggers anaphase in yeast. Cell *103*, 375-386.

Umezu, K., Sugawara, N., Chen, C., Haber, J.E., and Kolodner, R.D. (1998). Genetic analysis of yeast RPA1 reveals its multiple functions in DNA metabolism. Genetics *148*, 989-1005.

Unal, E., Arbel-Eden, A., Sattler, U., Shroff, R., Lichten, M., Haber, J.E., and Koshland, D. (2004). DNA damage response pathway uses histone modification to assemble a double-strand break-specific cohesin domain. Mol Cell *16*, 991-1002.

Unal, E., Heidinger-Pauli, J.M., Kim, W., Guacci, V., Onn, I., Gygi, S.P., and Koshland, D.E. (2008). A molecular determinant for the establishment of sister chromatid cohesion. Science *321*, 566-569.

Unal, E., Heidinger-Pauli, J.M., and Koshland, D. (2007). DNA double-strand breaks trigger genome-wide sister-chromatid cohesion through Eco1 (Ctf7). Science *317*, 245-248.

Usui, T., Ohta, T., Oshiumi, H., Tomizawa, J., Ogawa, H., and Ogawa, T. (1998). Complex formation and functional versatility of Mre11 of budding yeast in recombination. Cell *95*, 705-716.

van Attikum, H., Fritsch, O., and Gasser, S.M. (2007). Distinct roles for SWR1 and INO80 chromatin remodeling complexes at chromosomal double-strand breaks. Embo J *26*, 4113-4125.

Wang, X., and Haber, J.E. (2004). Role of *Saccharomyces* single-stranded DNA-binding protein RPA in the strand invasion step of double-strand break repair. PLoS Biol *2*, E21.

Wang, X., Ira, G., Tercero, J.A., Holmes, A.M., Diffley, J.F., and Haber, J.E. (2004). Role of DNA replication proteins in DSB-induced recombination in *S. cerevisiae*. Mol Cell Biol *24*, 6891-6899.

Williams, R.S., Dodson, G.E., Limbo, O., Yamada, Y., Williams, J.S., Guenther, G., Classen, S., Glover, J.N., Iwasaki, H., Russell, P*., et al.* (2009). Nbs1 flexibly tethers Ctp1 and Mre11-Rad50 to coordinate DNA double-strand break processing and repair. Cell *139*, 87-99.

Williams, R.S., Moncalian, G., Williams, J.S., Yamada, Y., Limbo, O., Shin, D.S., Groocock, L.M., Cahill, D., Hitomi, C., Guenther, G*., et al.* (2008). Mre11 dimers coordinate DNA end bridging and nuclease processing in double-strand-break repair. Cell *135*, 97-109.

Wiltzius, J.J., Hohl, M., Fleming, J.C., and Petrini, J.H. (2005). The Rad50 hook domain is a critical determinant of Mre11 complex functions. Nat Struct Mol Biol *12*, 403-407.

Xu, X., Vaithiyalingam, S., Glick, G.G., Mordes, D.A., Chazin, W.J., and Cortez, D. (2008). The basic cleft of RPA70N binds multiple checkpoint proteins, including RAD9, to regulate ATR signaling. Mol Cell Biol *28*, 7345-7353.

Zou, L., and Elledge, S.J. (2003). Sensing DNA damage through ATRIP recognition of RPA-ssDNA complexes. Science *300*, 1542-1548.

Zou, Y., Liu, Y., Wu, X., and Shell, S.M. (2006). Functions of human replication protein A (RPA): from DNA replication to DNA damage and stress responses. J Cell Physiol *208*, 267-273.

Figure legends

Figure 1. *rfa1-t11* is checkpoint proficient and is epistatic with loss of MRX on HU

(A) Diagram of the three subunits of RPA. Rfa1 (*Sc*RPA70*)* contains 4 oligonucleotide binding (OB) domains. Unlike the others, the N-OB binds DNA poorly, but binds proteins. (B) Crystal structure of budding yeast Rfa1-t11$_{1\text{-}132}$ in cartoon with the five-stranded β-barrel forming the OB-fold colored in dark green. Residues 1-4 are not shown. The E45 side chain is indicated in blue atom colors while helices and coiled elements are in pale yellow. * = putative MRX-binding site. The right panel shows E45 in the Rfa1-t11$_{1\text{-}132}$ structure with residues R44, K45E and R62 displayed as sticks and blue atom colors. K45E disrupts this basic patch. (C) Western blot showing Rad53 phosphorylation upshift after release from α-factor into 0.2 M HU in wt and *rfa1-t11* strains*.* (D) Heat maps of Pearson correlation coefficients showing patterns of synergism between 1311 nuclear proteins in 0 and 20 mM HU. Red indicates a correlation while green indicates an anti-correlation. Black ring highlights the strong correlation between *rfa1-t11* and *mre11Δ.* (E,F) 10x dilution series showing epistasis of MRX components with *rfa1-t11* on genotoxic drugs, and additivity with *mec1-100* and *rad51Δ*. All strains are *RAD5+* isogenic strains (Table S1).

Figure 2. Resumption of replication after HU-induced stalling fails in the *rfa1-t11* mutant

(A) Recovery assay after G1 arrest with α-factor and release into 0.2 M HU of indicated mutants (*rfa1-t11, mre11Δ* and *mec1-100; n=3*). (B) ChIP of DNA polα at either the early firing ARS607 or late firing ARS501 (Cobb et al., 2003) after release from G1 arrest into in 0.2 M HU, *n=3.* (C) Experimental scheme of DNA combing: synchronized cells were released into 0.2 M HU for 90

min after which the HU is washed out and the cells are allowed to recover in fresh media containing a BrdU analog. DNA was combed and new synthesis was visualized by antibodies against BrdU and DNA. (D) Example images of DNA combing with gaps (white arrows) and shorter lengths of newly synthesized DNA in mutant backgrounds. (E) Cumulative frequency graph showing the non-replicated fiber fraction in wt and mutant strains. (F) Rad50-PK ChIP to ARS607 after release from α-factor into 0.2 M HU, n=3. (G) Example plots of genome-wide Rad50-PK ChIP-chip showing loss of Rad50 at origins 307-309 in *rfa1-t11*. (H) Box plots of Rad50 ChIP-chip signals at all origins after release in to 0.2 M HU for 60 min at 25°C, in indicated strains. Error bars represent the SEM. (I) Model placing *rfa1-t11* on a pathway with MRX, parallel to Mec1 activation, to confer replication fork integrity.

Figure 3. The interaction between MRX and Rfa1 is disrupted in *rfa1-t11*

(A) Western blot showing that the Rfa1 antibody recognizes the N-OB of both Rfa1 and rfa1-t11 equally. (B,C) Co-IP from yeast extracts of indicated mutants using either antibodies against the PK tag, Xrs2 or Rfa1. Samples were Benzonase treated (Fig S3A). (D) Scheme of MRX scanning peptide microarray probed with N-OB of either Rfa1 or rfa1-t11. 206 peptides (18 aa each) were spotted on to a glass slide for binding to Rfa1 or rfa1-t11 N-OB from (A). Supplemental Exp. Procedures describe signal detection and quantitation. (E) Interaction heat maps for either Rfa1 or rfa1-t11 across MRX. Arrows indicate regions of strong (red) binding sensitive to the *rfa1-t11* mutation, n=3. (F) Crystal structure of *Chaetomium* Mre11-Rad50 dimer with dsDNA (Seifert et al., 2015). Peptides scored in the microarray as strongly interacting with RFA1 OB fold domain are highlighted in red. (G) Purified Rfa1-N (dilution series from 0.12 to 1000 μM) was incubated with 25 μM Cy5-labeled Rad50 and Mre11 peptides for 15 min at rt. Dissociation

constant K_d of 63.6 ± 7 μM is for Rad50 peptide 17 and Rfa1-N (n=3), error bars represent SEM, ΔF_{norm} (‰) represents change in fluorescence during thermophoresis normalized to initial fluorescence). Detailed list of peptides in Table S2.

Figure 4. *rfa1-t11* has a diminished checkpoint response to DSBs but resection is intact

(A) 10x dilution series on YPAD ± HU and Zeocin of isogenic strains with the indicated genotypes. (B) Western blot showing Rad53 phosphorylation upshift after release from α-factor into 250 μg/ml Zeocin. No Rad53 phosphorylation was detectable in *tel1Δ rfa1-t11*. Mcm2 is the loading control. (C) γH2A ChIP to a HO-induced DSB at *MATα* (van Attikum et al., 2007) at 120 min after cut induction, *n=4.* (D) Cut efficiency time course from (Fig. 5A) showing that wt and *rfa1-t11* have similar cut efficiencies. After replication, both sisters are likely to be cut at once. (E) QAOS assay showing equal accumulation of ssDNA at 1.6kb from the DSB at *MATα* in wt and *rfa1-t11,* reproduced from (Dubrana et al., 2007). Error bars represent SEM.

Figure 5. *rfa1-t11* reduces the recruitment of MRX to DSBs

(A) Rad50-PK ChIP at an HO-induced DSB at *MATα* on Chr3 in asynchronous cells, n=5 (for probes, van Attikum et al., 2007). HO cut efficiencies for each experiment are in Table S3. We assume that both sisters are cut, given the high rate of cleavage scored for individual loci. (B) Mre11-YFP foci accumulation after 250 μg/ml Zeocin, *n*≥65. Details in Table S4. (C) Scc1-HA ChIP to an HO-induced DSB at 120 min after induction, *n=4* as (A). (D) Scheme of the NHEJ repair pathways that yield either *URA*- (imprecise end-joining) or *URA+* (precise end-joining) phenotypes (Matsuzaki et al., 2012). Graph shows the % *URA*- and *URA+* survivors in various genotypes, n=3. Error bars represent SEM except for (B), where they are the SD.

Figure 6. RFA1-mediated recruitment of MRX to DSBs is necessary for tethering ends and sister chromatids

(A) Scheme of strain used for tracking both sides of a galactose inducible I-SceI DSB on Chr2. LacO/LacI-GFP tags one side and TetO/TetR-CFP the other (Lobachev et al., 2004). MRX can tether ends through Rad50's hook domain by directly binding to the DSB end or by interaction with RPA. Examples of separation of GFP/CFP signals after I-SceI cut induction. Graph shows the percentage separated GFP/CFP in large budded cells, $n \geq 107$. For details and statistics see Table S4. Cells scored were late G2/M (large bud and SPBs < 0.6 µm apart). For uncleaved controls, mid-S and G2/M cells were scored. (B) Construct used to measure sister chromatid pairing at an HO-induced DSB. Cut efficiencies are scored for each experiment (Table S3). MRX can hold sister chromatids together at DSBs through Rad50 hook-hook interactions or its ring structure. (C) Examples of brightfield/GFP merged SIM images of wt and *rfa1-t11* fixed cells bearing the construct at time indicated after cleavage induction (B). Insets show enlarged LacI-GFP foci (bar=0.5 µm). The focus area is quantified by Fiji (Table S4). Fully separated foci were never observed in wt S-phase cells and rarely in *rfa1-t11* cells. Foci were nonuniform in *rfa1-t11* and *rad50Δ*. (D) Boxplots of LacI-GFP spot areas before and after 1h TEV induction (upper plot) or 2h after HO cut (lower three plots), $n \geq 35$. Full statistics in Table S4.

Figure 7. MRX is sufficient and necessary to hold sister chromatids together at DSBs

(A) Construct used to measure changes in sister chromatid pairing at a HO induced DSB at *MATα*. Cohesin binding is later and more distant from the cut site. Right panel is an example kymograph of live cell imaging of a LacI-GFP spot projected through the x axis over time in wt

versus *rfa1-t11* after 120 min galactose induction of HO. Black arrows indicate separation events. Uncut conditions are on glucose. (B, C) Quantitation of the number of frames containing 2 LacI-GFP spots at either 25°C or 37°C, *n≥5.* All details and statistics are in Table S4, and example movies are online. (D) Experimental layout for the sister chromatid cohesion assay using the construct in (A) and *MATa*^{inc} for an uncut locus. Asynchronous cultures of indicated mutants were grown at 25°C until log phase, 15 µg/ml Nocodazole and either glucose (no cut) or galactose (cut) were added. Growth for 1 h preceded a shift to 37°C and fixation. (E, F) Quantitation of the number of G2/M cells with separated sister chromatids (2 spots) in the indicated isogenic strains carrying the construct in (A), *n≥201* (Table S4 for statistics). Asterisks indicate a p value < 0.005. HO cut efficiencies are in Table S3.

Table 1 - Crystallographic data collection and refinement statistics

	Rfa1-t11$_{1-132}$ Se-Met peak[a]
Data collection	
Space group	P 2_1
Unit cell dimensions	
a, *b*, *c* (Å)	29.62, 115.35, 69.03
α, β, γ (°)	90.0, 90.7, 90.0
Resolution range (Å)[b]	50.0 – 1.8 (1.85-1.80)
Wavelength (Å)	0.97941
Completeness (%)[b]	95.4 (86.2)
Redundancy[b]	2.4 (2.3)
R_{sym}[b]	0.079 (0.527)
$I/\sigma(I)$[b]	8.0 (1.7)
CC (1/2) (%)[b]	99.5 (67.9)
Unique reflections	80762
Refinement	
R_{work}	0.164
R_{free}	0.214
Resolution range (Å)	44.3 – 1.8

Rfa1-t11$_{1-132}$ Se-Met peak[a]	
Data collection	
Space group	P 2_1
Reflections (all)	41721
Reflections (test set)	2086 (5%)
Number of atoms	4246
Figure of merit	0.415
***B*-Factors** (Å^2)	
Overall	31.7
Protein	31.0
Solvent	39.4
RMS Deviations	
Bond lengths (Å)	0.01
Bond angles (°)	1.05
Ramachandran plot	
Allowed (%)	100.0
Outliers (%)	0.0

[a] Data collection statistics is reported for unmerged reflections

[b] Values in parentheses refer to the highest resolution shell

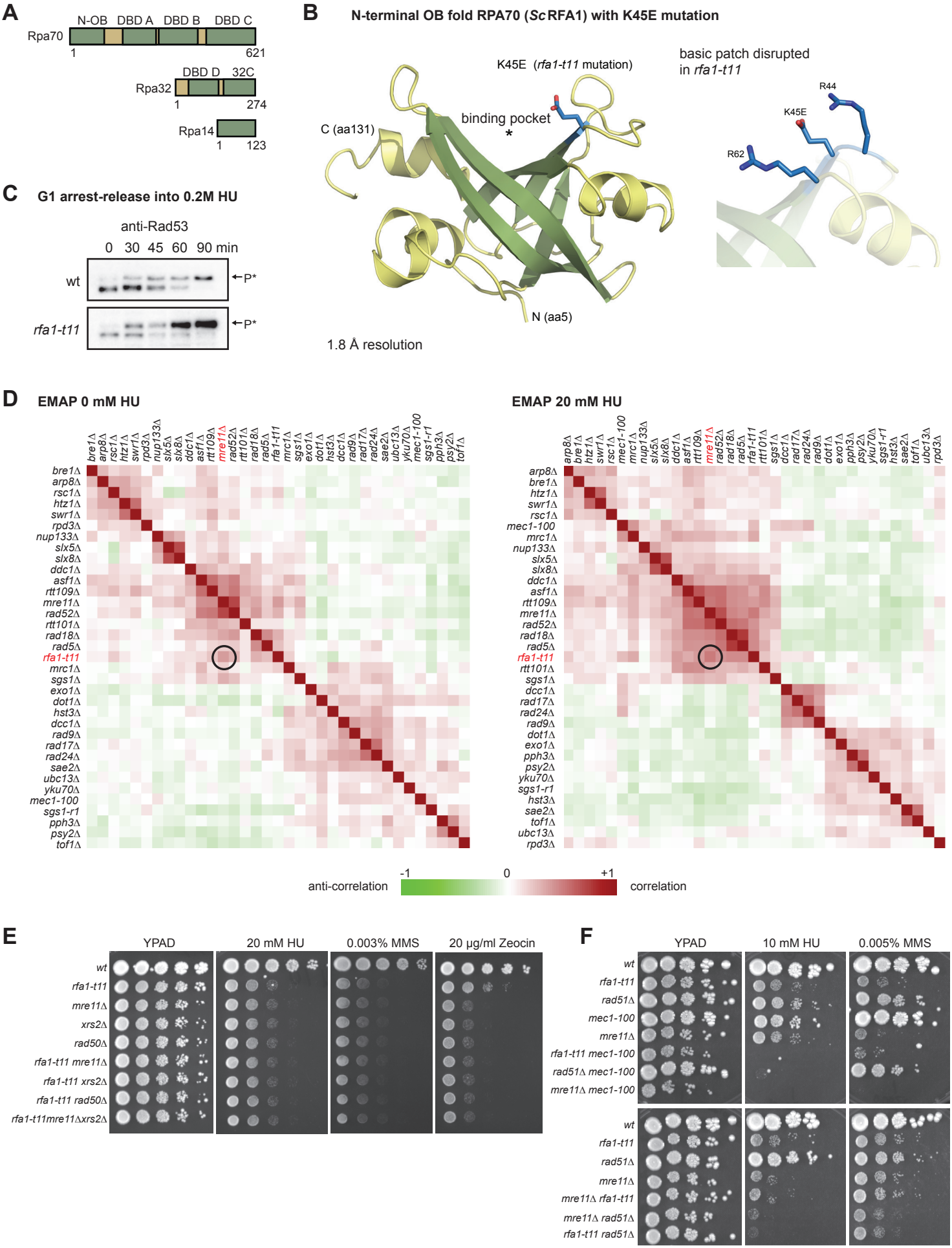
A
N-OB DBD A DBD B DBD C
Rpa70
1
621
DBD D 32C
Rpa32
1
274
Rpa14
1
123
B
N-terminal OB fold RPA70 (ScRFA1) with K45E mutation
K45E (rfa1-t11 mutation)
basic patch disrupted in rfa1-t11
C (aa131)
binding pocket
*
R44
K45E
R62
N (aa5)
1.8 Å resolution
C
G1 arrest-release into 0.2M HU
anti-Rad53
0 30 45 60 90 min
wt
rfa1-t11
P*
D
EMAP 0 mM HU
EMAP 20 mM HU
anti-correlation
-1
0
+1
correlation
E
YPAD
20 mM HU
0.003% MMS
20 µg/ml Zeocin
wt
rfa1-t11
mre11Δ
xrs2Δ
rad50Δ
rfa1-t11 mre11Δ
rfa1-t11 xrs2Δ
rfa1-t11 rad50Δ
rfa1-t11mre11Δxrs2Δ
F
YPAD
10 mM HU
0.005% MMS
wt
rfa1-t11
rad51Δ
mec1-100
mre11Δ
rfa1-t11 mec1-100
rad51Δ mec1-100
mre11Δ mec1-100
wt
rfa1-t11
rad51Δ
mre11Δ
mre11Δ rfa1-t11
mre11Δ rad51Δ
rfa1-t11 rad51Δ

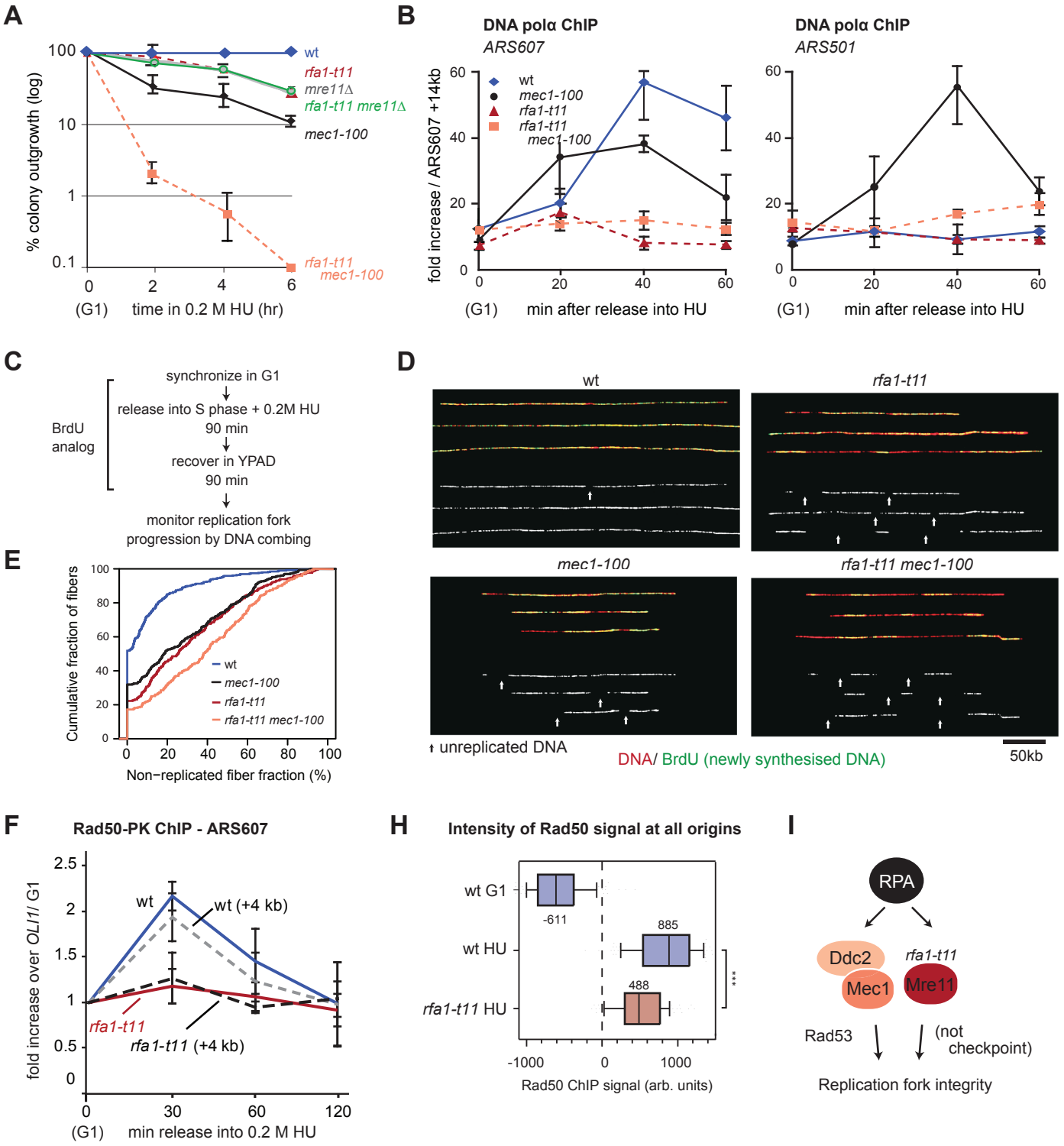
A
% colony outgrowth (log)
wt
rfa1-t11
mre11Δ
rfa1-t11 mre11Δ
mec1-100
rfa1-t11 mec1-100
(G1) time in 0.2 M HU (hr)
B
DNA polα ChIP
ARS607
fold increase / ARS607 +14kb
wt
mec1-100
rfa1-t11
rfa1-t11 mec1-100
(G1) min after release into HU
DNA polα ChIP
ARS501
(G1) min after release into HU
C
BrdU analog
synchronize in G1
release into S phase + 0.2M HU 90 min
recover in YPAD 90 min
monitor replication fork progression by DNA combing
D
wt
rfa1-t11
mec1-100
rfa1-t11 mec1-100
unreplicated DNA
DNA/ BrdU (newly synthesised DNA)
50kb
E
Cumulative fraction of fibers
wt
mec1-100
rfa1-t11
rfa1-t11 mec1-100
Non−replicated fiber fraction (%)
F
Rad50-PK ChIP - ARS607
fold increase over OLI1/ G1
wt
wt (+4 kb)
rfa1-t11
rfa1-t11 (+4 kb)
(G1) min release into 0.2 M HU
H
Intensity of Rad50 signal at all origins
wt G1
wt HU
rfa1-t11 HU
-611
885
488
***
Rad50 ChIP signal (arb. units)
I
RPA
Ddc2
Mec1
rfa1-t11
Mre11
Rad53
(not checkpoint)
Replication fork integrity
G
ChIP-Chip for Rad50 in RFA1 and rfa1-t11 cells arrested in HU
ARS307
ARS308
ARS309
RFA1
rfa1-t11
Signal log2 ratio
Position on Chr3 (kb)

Figure

Seeber et al Figure 3

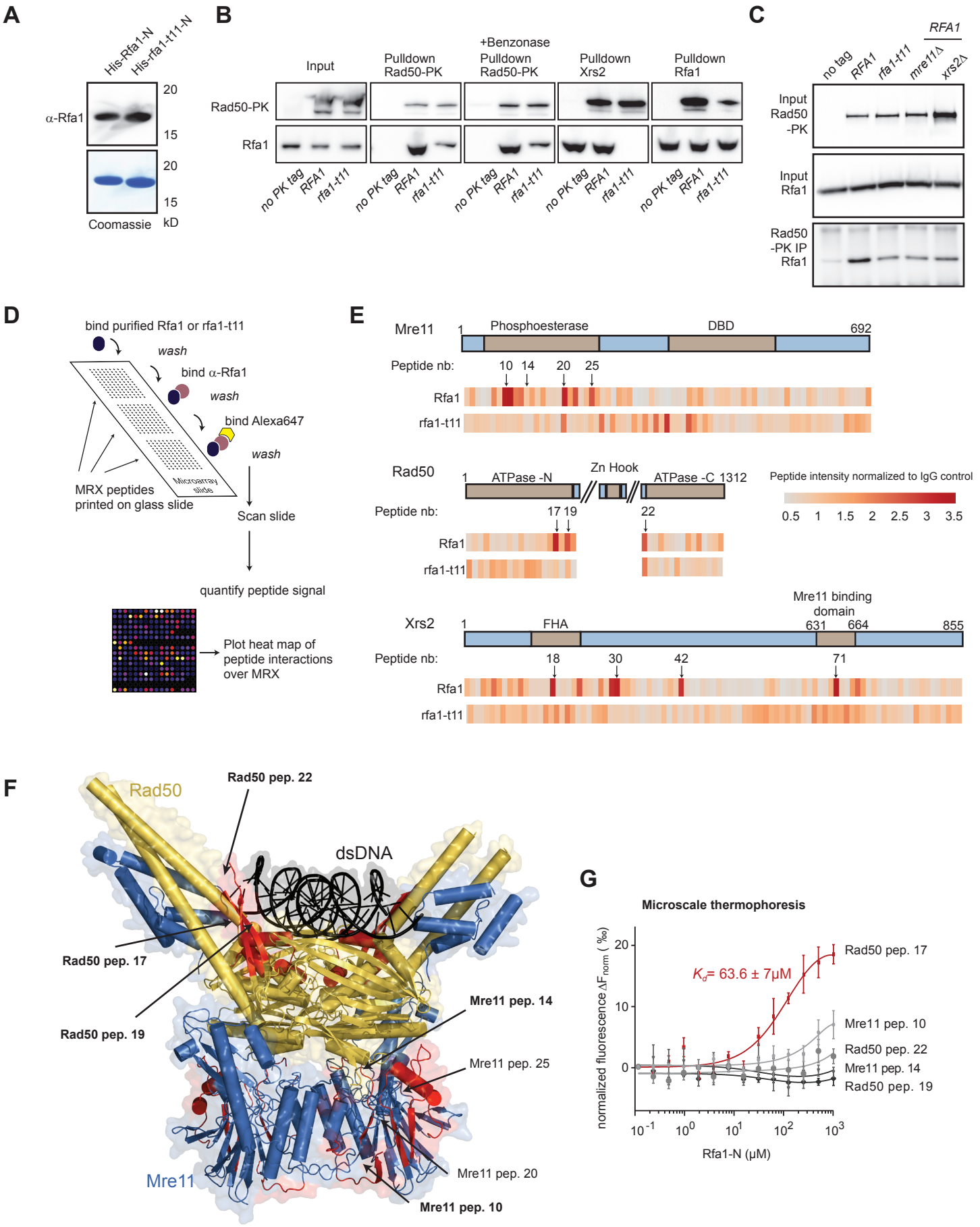

Figure

Seeber et al Figure 4

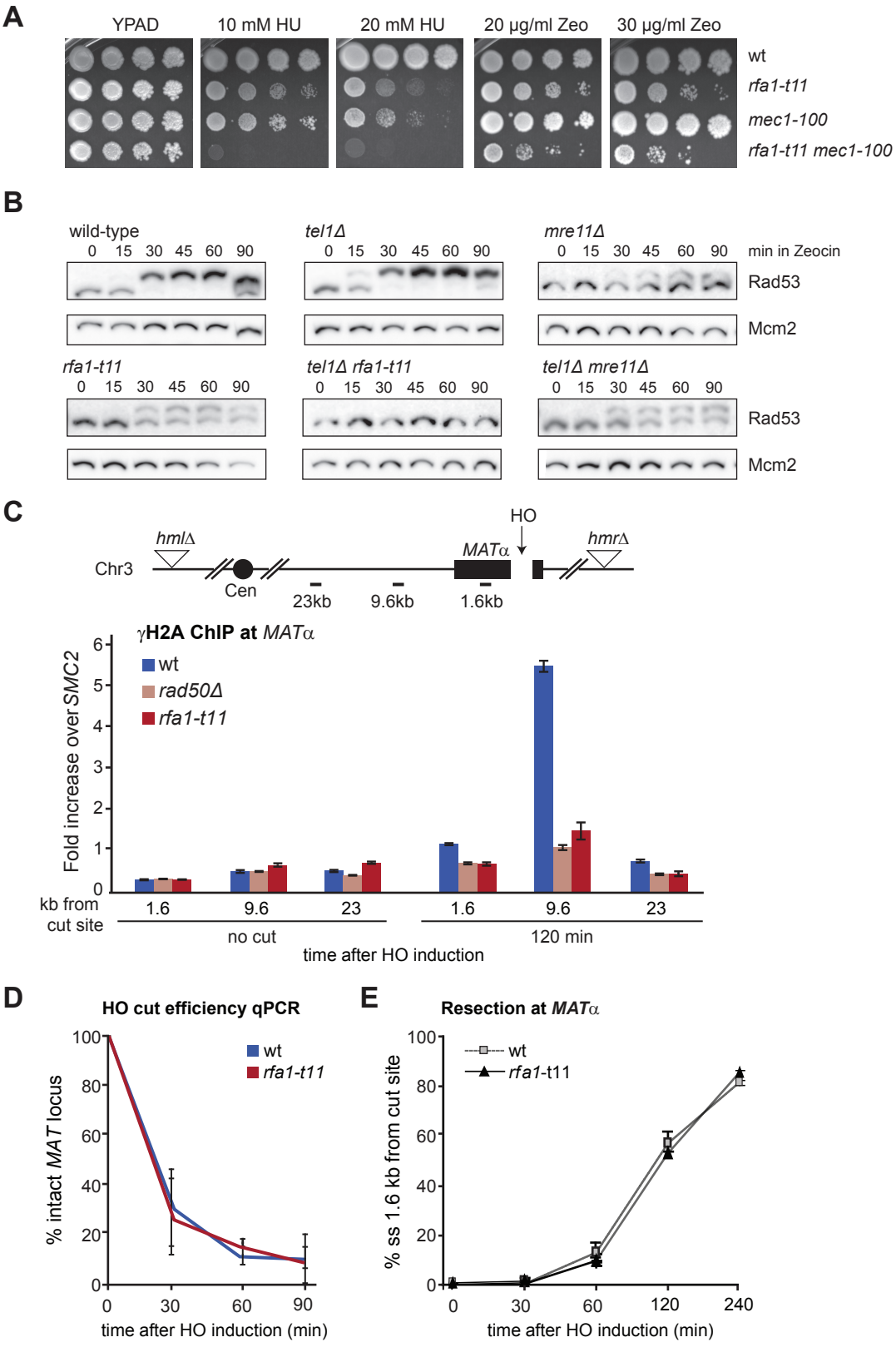

Figure

Seeber et al Figure 5

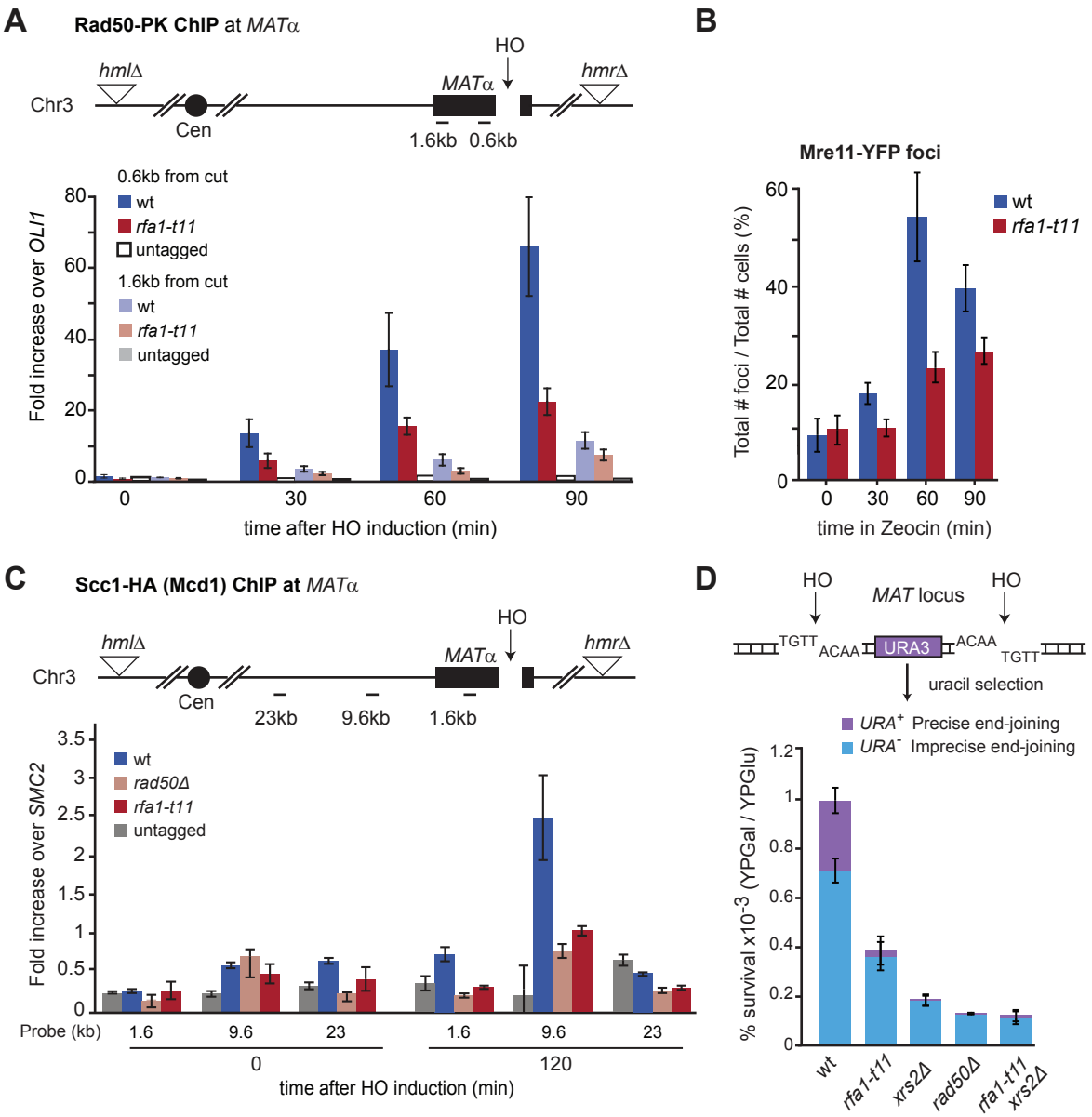

A **End-to-end tethering**

+ Spc29-RFP (spindle pole body)
+ *GAL1-10 I-SceI*

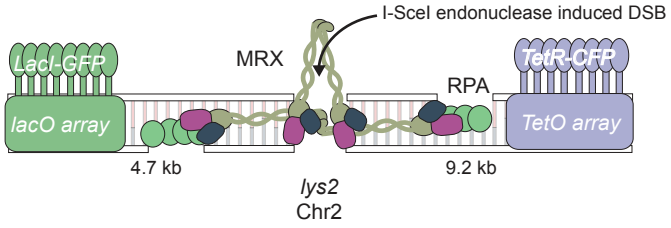

G2/M arrested cells 4 hr after I-SceI induction

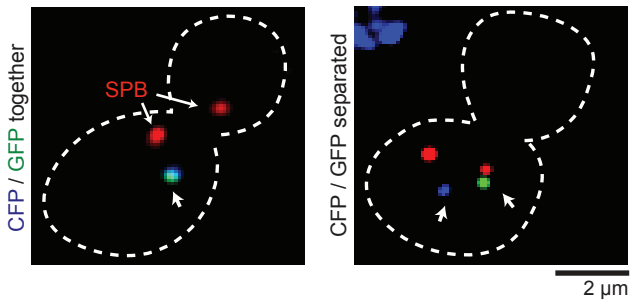

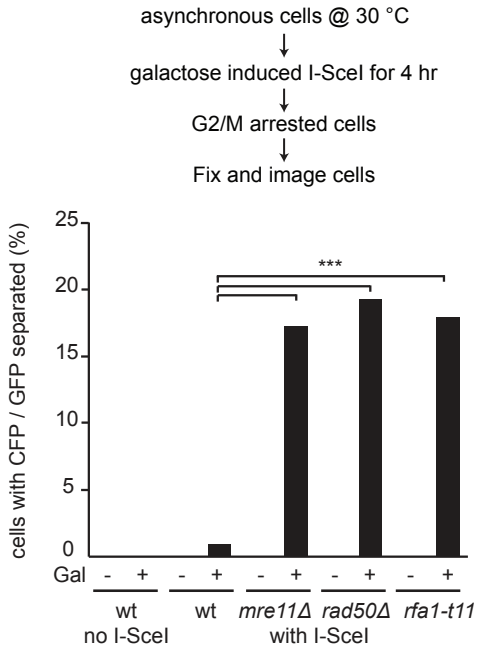

B **Sister chromatid cohesion**

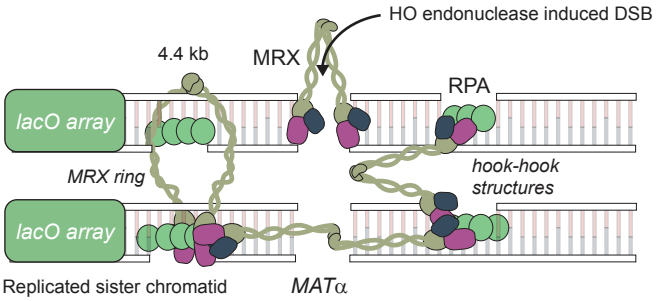

C **Structured illumination microscopy (SIM) of fixed cells**

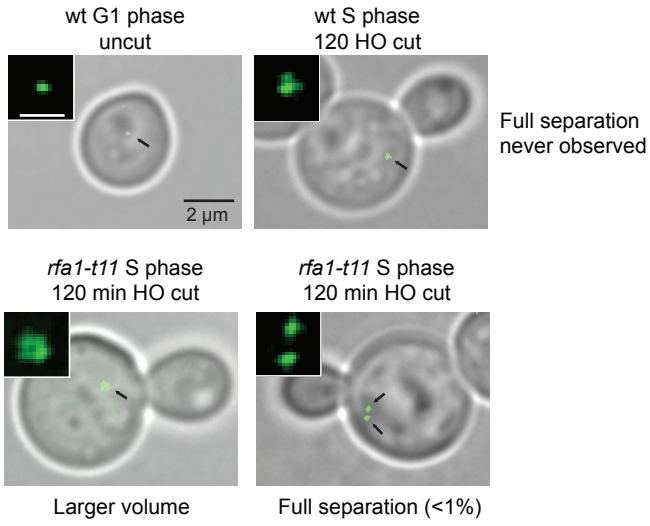

D **Quantification of single-spot volume by SIM**

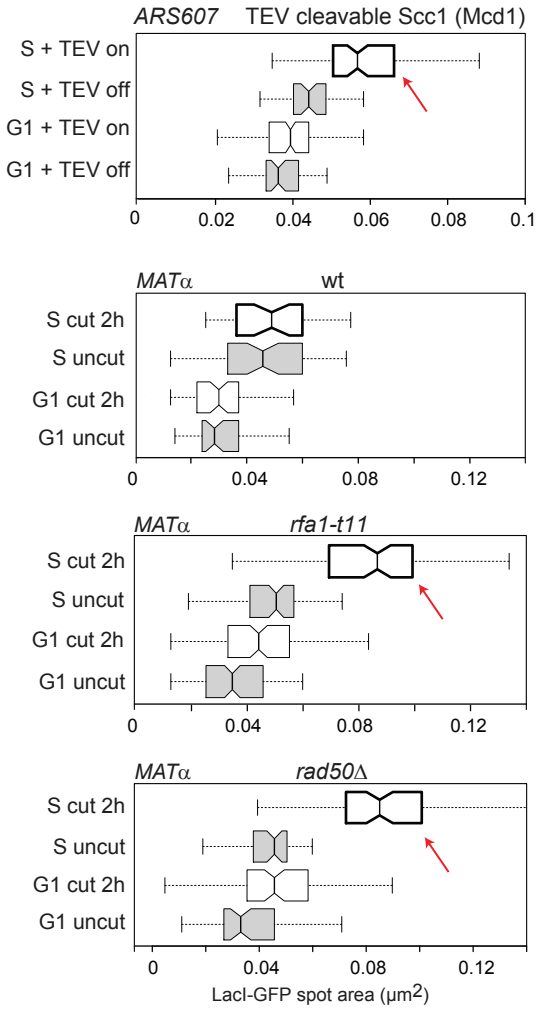

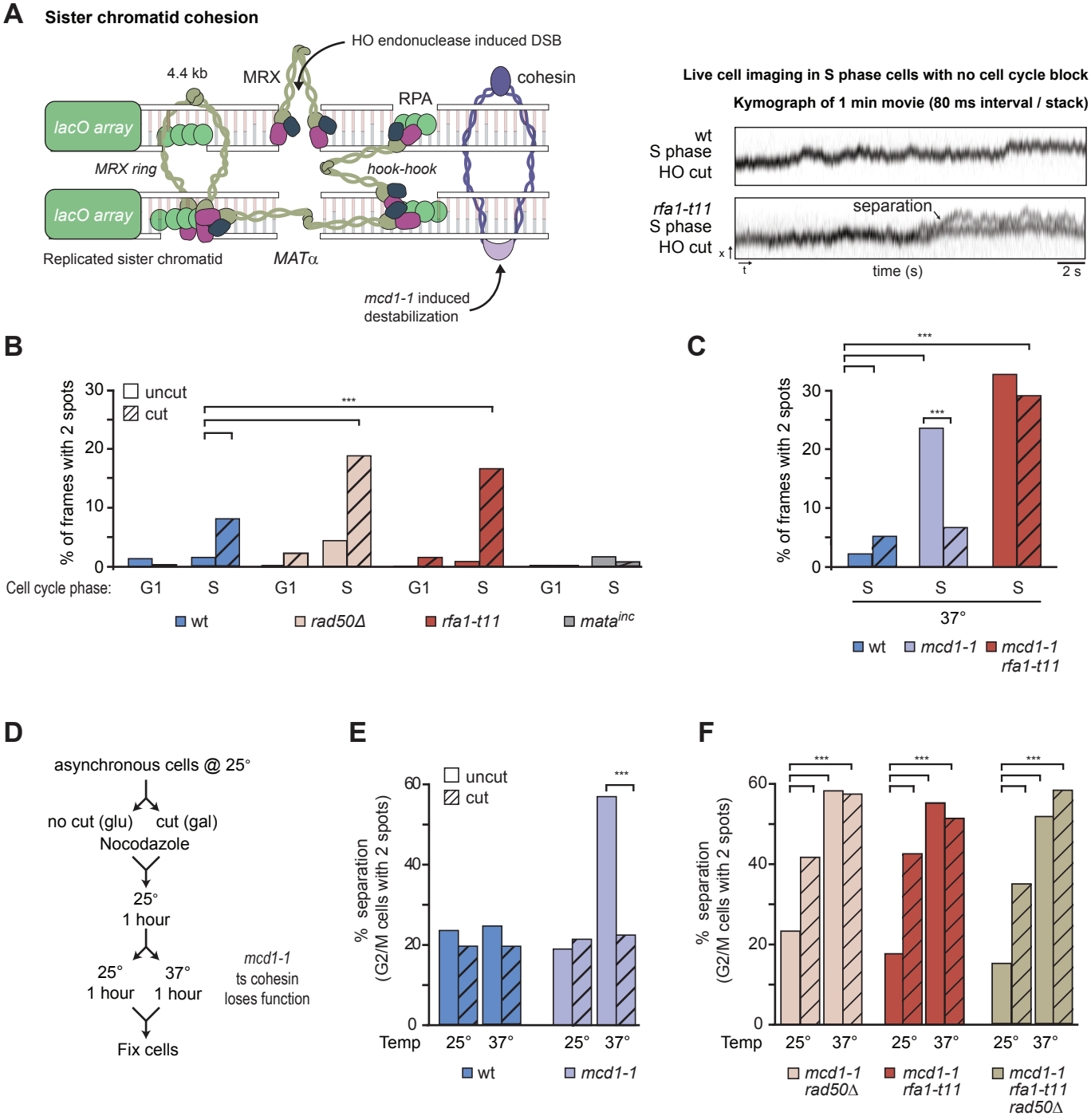
A
Sister chromatid cohesion
HO endonuclease induced DSB
4.4 kb
MRX
cohesin
RPA
lacO array
MRX ring
hook-hook
lacO array
Replicated sister chromatid
MATα
mcd1-1 induced destabilization
Live cell imaging in S phase cells with no cell cycle block
Kymograph of 1 min movie (80 ms interval / stack)
wt
S phase
HO cut
rfa1-t11
S phase
HO cut
separation
x
t
time (s)
2 s
B
% of frames with 2 spots
uncut
cut
***
Cell cycle phase:
G1
S
wt
rad50Δ
rfa1-t11
mata^inc
C
% of frames with 2 spots
***
S
37°
wt
mcd1-1
mcd1-1 rfa1-t11
D
asynchronous cells @ 25°
no cut (glu)
cut (gal)
Nocodazole
25°
1 hour
25°
1 hour
37°
1 hour
Fix cells
mcd1-1
ts cohesin
loses function
E
% separation (G2/M cells with 2 spots)
uncut
cut
***
Temp
25°
37°
wt
mcd1-1
F
% separation (G2/M cells with 2 spots)
***
Temp
25°
37°
mcd1-1 rad50Δ
mcd1-1 rfa1-t11
mcd1-1 rfa1-t11 rad50Δ

Seeber et al Suppl Figure S1

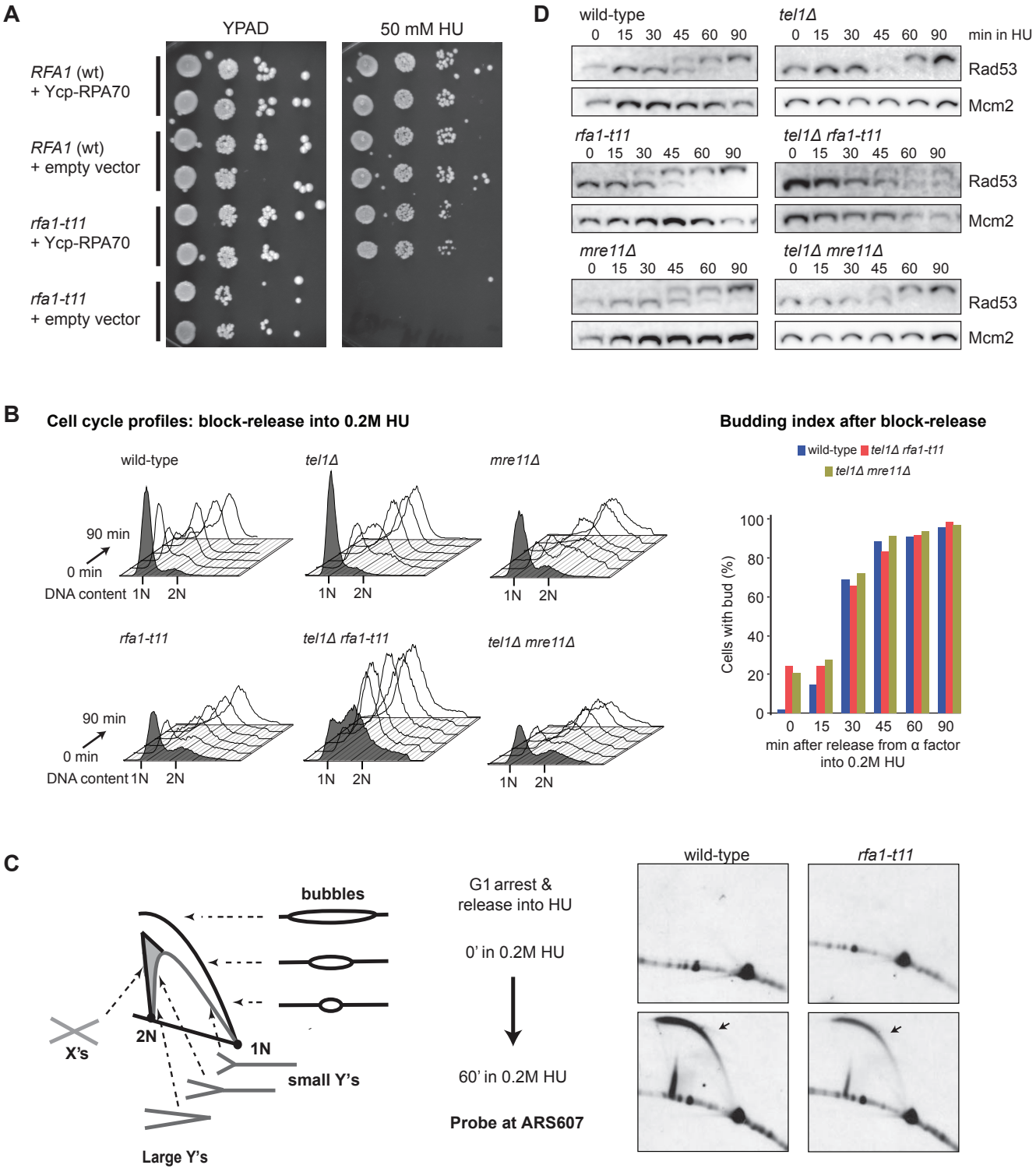

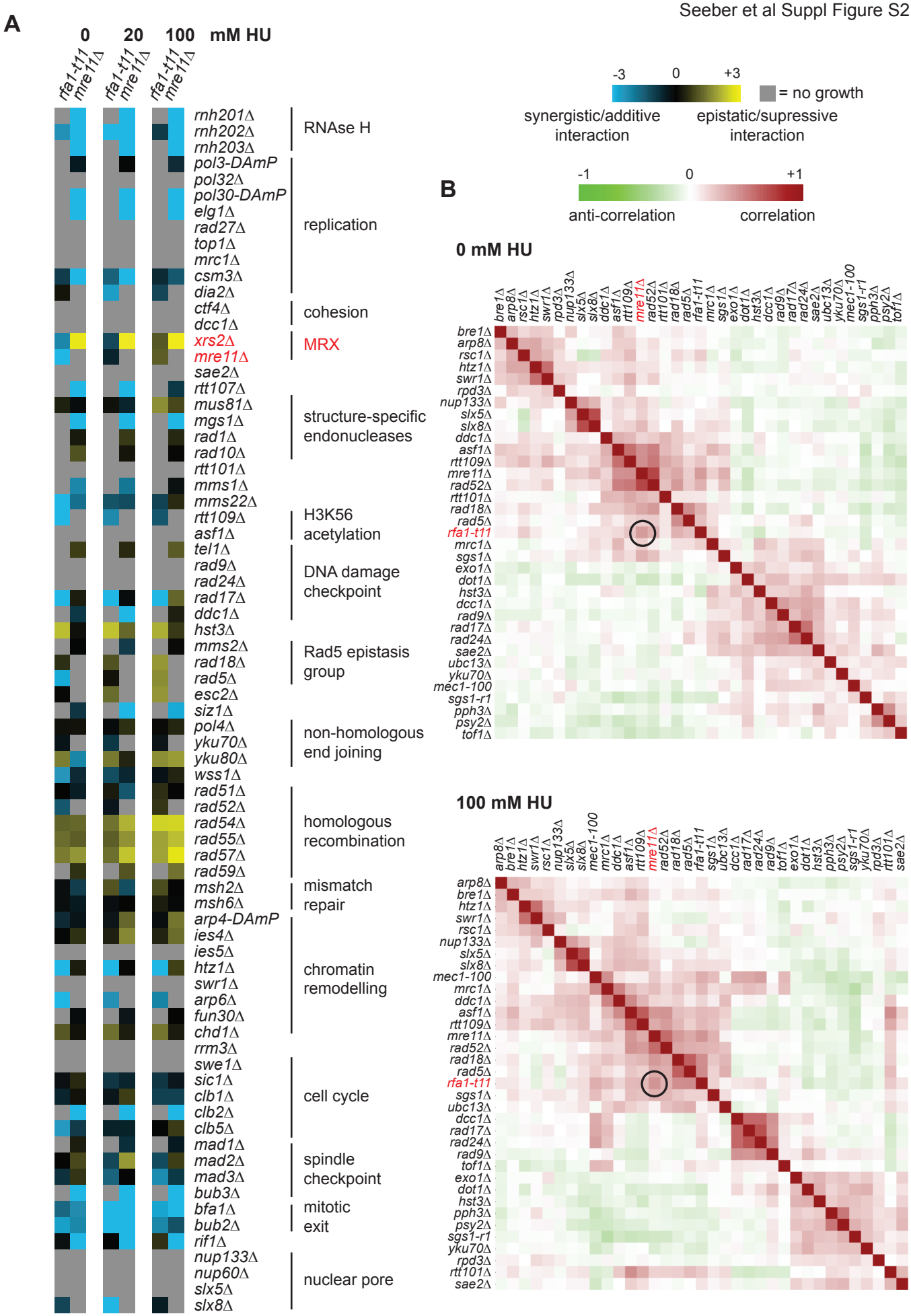
A
0
20
100
mM HU
rfa1-t11
mre11Δ
rnh201Δ
rnh202Δ
rnh203Δ
pol3-DAmP
pol32Δ
pol30-DAmP
elg1Δ
rad27Δ
top1Δ
mrc1Δ
csm3Δ
dia2Δ
ctf4Δ
dcc1Δ
xrs2Δ
mre11Δ
sae2Δ
rtt107Δ
mus81Δ
mgs1Δ
rad1Δ
rad10Δ
rtt101Δ
mms1Δ
mms22Δ
rtt109Δ
asf1Δ
tel1Δ
rad9Δ
rad24Δ
rad17Δ
ddc1Δ
hst3Δ
mms2Δ
rad18Δ
rad5Δ
esc2Δ
siz1Δ
pol4Δ
yku70Δ
yku80Δ
wss1Δ
rad51Δ
rad52Δ
rad54Δ
rad55Δ
rad57Δ
rad59Δ
msh2Δ
msh6Δ
arp4-DAmP
ies4Δ
ies5Δ
htz1Δ
swr1Δ
arp6Δ
fun30Δ
chd1Δ
rrm3Δ
swe1Δ
sic1Δ
clb1Δ
clb2Δ
clb5Δ
mad1Δ
mad2Δ
mad3Δ
bub3Δ
bfa1Δ
bub2Δ
rif1Δ
nup133Δ
nup60Δ
slx5Δ
slx8Δ
RNAse H
replication
cohesion
MRX
structure-specific endonucleases
H3K56 acetylation
DNA damage checkpoint
Rad5 epistasis group
non-homologous end joining
homologous recombination
mismatch repair
chromatin remodelling
cell cycle
spindle checkpoint
mitotic exit
nuclear pore
-3
0
+3
= no growth
synergistic/additive interaction
epistatic/supressive interaction
B
-1
0
+1
anti-correlation
correlation
0 mM HU
100 mM HU

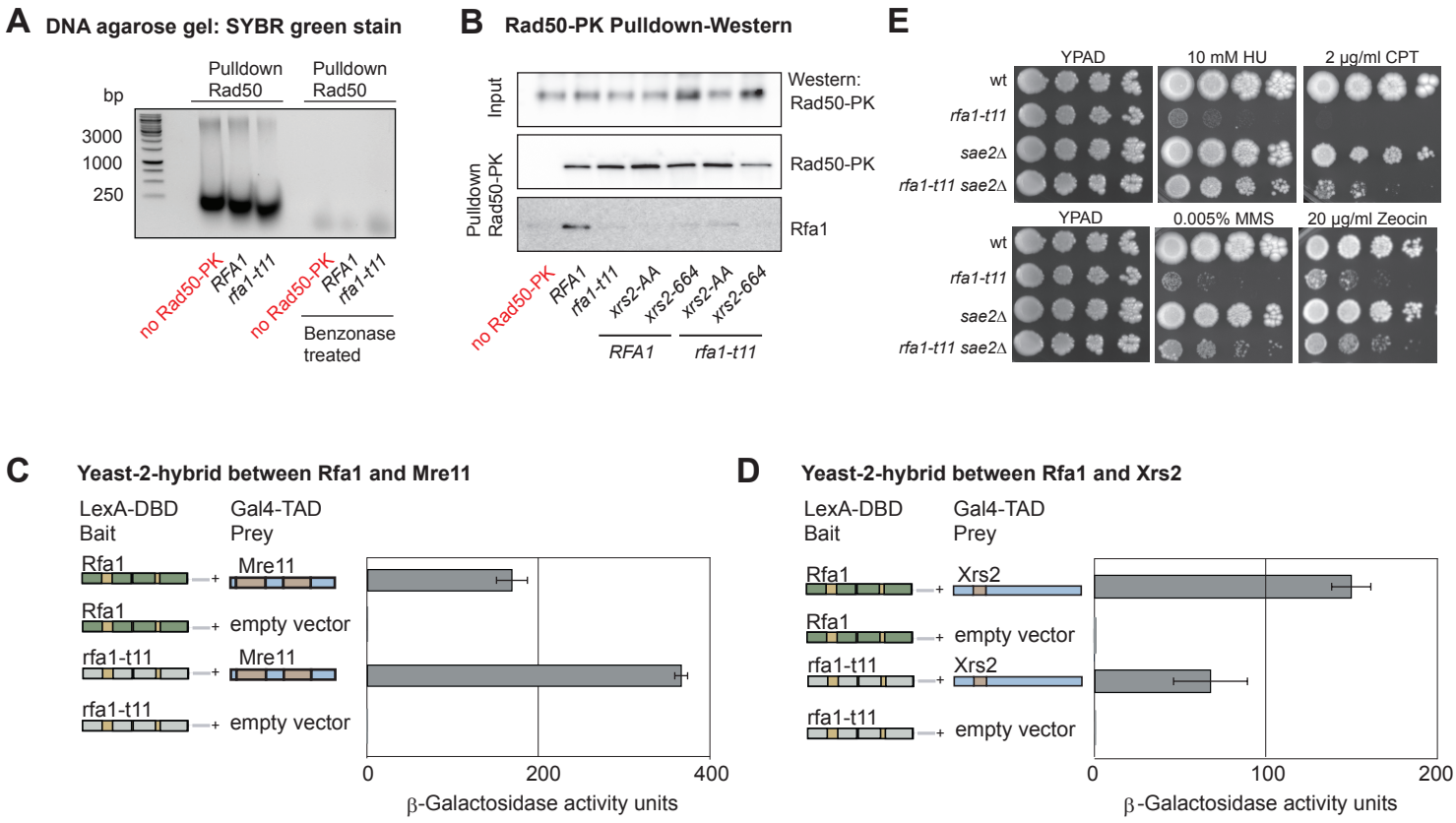
A
DNA agarose gel: SYBR green stain
bp
3000
1000
250
Pulldown Rad50
Pulldown Rad50
no Rad50-PK
RFA1
rfa1-t11
no Rad50-PK
RFA1
rfa1-t11
Benzonase treated
B
Rad50-PK Pulldown-Western
Input
Pulldown Rad50-PK
Western: Rad50-PK
Rad50-PK
Rfa1
no Rad50-PK
RFA1
rfa1-t11
xrs2-AA
xrs2-664
xrs2-AA
xrs2-664
RFA1
rfa1-t11
E
YPAD
10 mM HU
2 µg/ml CPT
wt
rfa1-t11
sae2Δ
rfa1-t11 sae2Δ
YPAD
0.005% MMS
20 µg/ml Zeocin
wt
rfa1-t11
sae2Δ
rfa1-t11 sae2Δ
C
Yeast-2-hybrid between Rfa1 and Mre11
LexA-DBD Bait
Gal4-TAD Prey
Rfa1
Mre11
Rfa1
empty vector
rfa1-t11
Mre11
rfa1-t11
empty vector
0
200
400
β-Galactosidase activity units
D
Yeast-2-hybrid between Rfa1 and Xrs2
LexA-DBD Bait
Gal4-TAD Prey
Rfa1
Xrs2
Rfa1
empty vector
rfa1-t11
Xrs2
rfa1-t11
empty vector
0
100
200
β-Galactosidase activity units

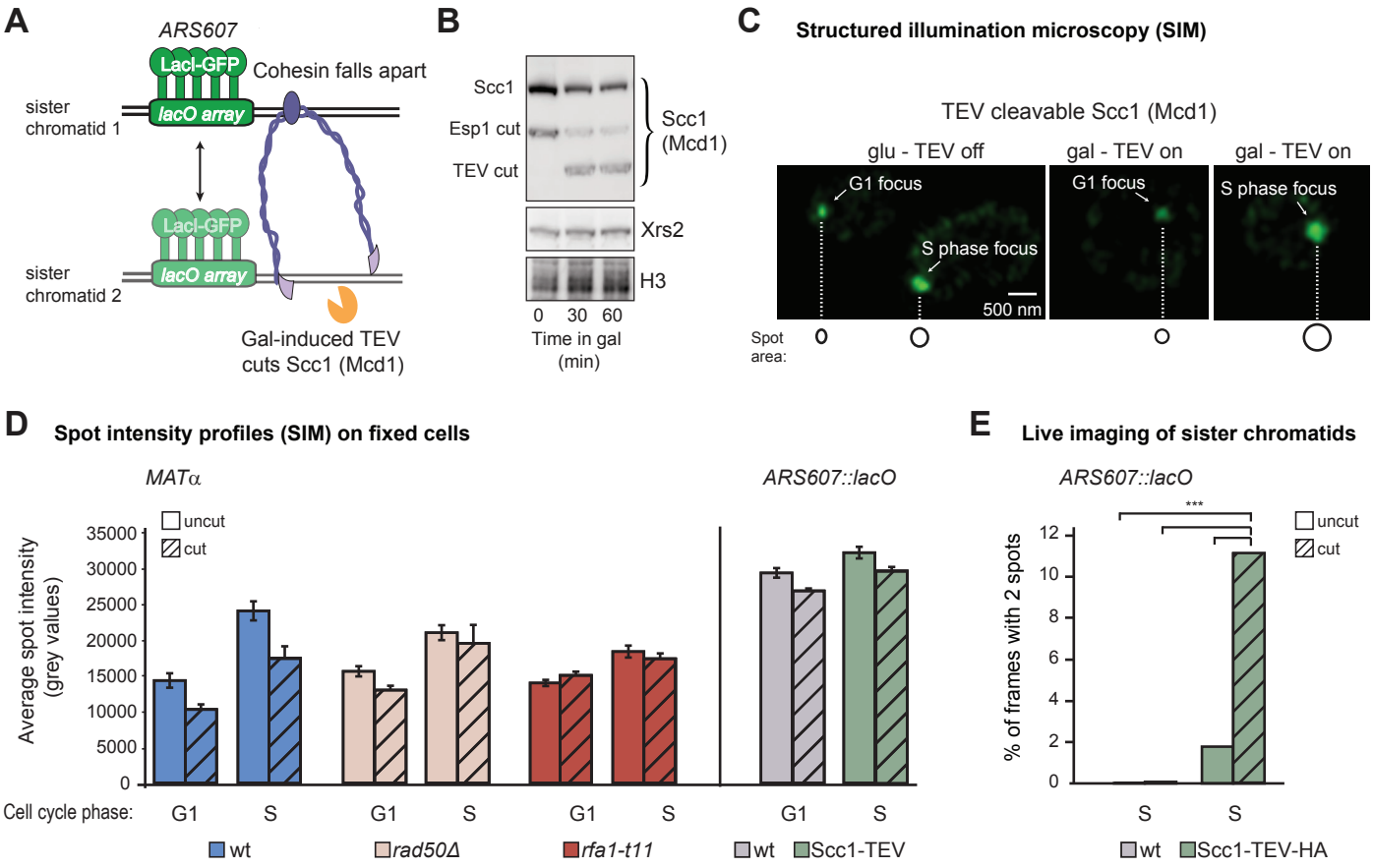
A
ARS607
LacI-GFP
Cohesin falls apart
sister chromatid 1
lacO array
LacI-GFP
sister chromatid 2
lacO array
Gal-induced TEV cuts Scc1 (Mcd1)
B
Scc1
Esp1 cut
TEV cut
Scc1 (Mcd1)
Xrs2
H3
0 30 60
Time in gal (min)
C
Structured illumination microscopy (SIM)
TEV cleavable Scc1 (Mcd1)
glu - TEV off
gal - TEV on
gal - TEV on
G1 focus
S phase focus
G1 focus
S phase focus
500 nm
Spot area:
D
Spot intensity profiles (SIM) on fixed cells
MATα
ARS607::lacO
Average spot intensity (grey values)
uncut
cut
35000
30000
25000
20000
15000
10000
5000
0
Cell cycle phase:
G1 S G1 S G1 S G1 S
wt
rad50Δ
rfa1-t11
wt
Scc1-TEV
E
Live imaging of sister chromatids
ARS607::lacO
% of frames with 2 spots
***
uncut
cut
12
10
8
6
4
2
0
S S
wt
Scc1-TEV-HA

Seeber et al., Supplemental Material

Supplemental Figures S1-S4

Supplemental Figure legends S1-S4

Supplemental Movie legend S1

Supplemental Tables and legends S1-S4, Tables S1, S2 and S4 are uploaded as separate files

Supplemental Experimental procedures

Supplemental References

Supplemental figure legends

Figure S1. The recessive mutation *rfa1-t11* progresses normally through unperturbed S phase, and supports both origin firing and checkpoint activation on HU, related to figure 1

(A) 10x dilution series on YPAD ± 50 mM HU for wild-type (wt) and *rfa1-t11* strains containing a plasmid expressing either a wild-type *RFA1*, *rfa1-t11* or empty vector, showing that *rfa1-t11* is a recessive mutation. (B) Cell cycle profiles of propidium iodide (PI) stained nuclei after release from α-factor into 0.2 M HU. Right panel is budding index of wild-type, *tel1Δ rfa1-t11* and *tel1Δ mre11Δ* cells showing similar release profiles, to confirm proper progression into S phase. (C) Illustration highlighting key features of a 2D gel. 2D gel images showing replication fork firing at ARS607 (see Supplemental experimental procedures) in wt and *rfa1-t11* in the presence of 0.2 M HU. Black arrows highlight replication bubble arcs. (D) Western blot showing Rad53 activation (phosphorylation upshift detected by antibody) after release from α-factor into 0.2 M HU in the indicated isogenic strains. Mcm2 is used as a loading control.

Figure S2. Quantitative genetic interaction mapping of 1311 query strains reveals an epistatic relationship between *rfa1-t11* and MRX mutants, related to figure 1

(A) EMAP results showing the growth of double mutants on 0, 20, 100 mM HU. Yellow indicates an epistatic/suppressive interaction. Blue indicates a synergistic/additive interaction. Grey squares represent no growth due to cell death. (B) Heat maps of Pearson correlation coefficients showing patterns of synergism between 1311 nuclear proteins in untreated and 100 mM HU conditions. Red indicates a correlation while green indicates an anti-correlation. Black ring highlights the strong correlation between *rfa1-t11* and *mre11Δ.* The 0 mM HU heat map is a duplication from Figure 1D to allow comparison with the 100 mM HU heat map.

Figure S3. MRX complex physical interactions with *rfa1-t11* and genetic interaction with *sae2Δ,* related to figure 3

(A) DNA agarose gel stained with SYBR green showing the effect of treatment of yeast extracts with 1250 units of Benzonase. These samples were used for immunoprecipitations in Fig. 3A. All subsequent yeast extracts treated with Benzonase prior to IP for 30 mins on ice. (B) Rad50-PK pulldown in wt, *rfa1-t11* and the indicated *xrs2* mutants: xrs2-AA consists of two point mutations that disrupt Mre11 binding and xrs2-664 is a truncation of its entire C-terminus but maintains partial Mre11 binding. (C,D) Yeast-2-hybrid between Rfa1 or rfa1-t11 and Mre11 or Xrs2. Error bars represent the SEM, *n=3.* (E) 10x dilution series on YPAD ± indicated amounts of HU, CPT, MMS and Zeocin in combinations of wild-type, *sae2Δ* and *rfa1-t11* strains.

Figure S4. TEV cleavage of Scc1 (Mcd1) results in expansion of a genetically tagged locus and uncoordinated sister chromatid dynamics, related to figure 4

(A) Construct illustrating galactose-inducible TEV protease which cuts Scc1, allowing sister chromatids to separate. (B) Time course Western blot after galactose induction of a strain bearing TEV protease, showing full length (FL) Scc1, the resulting fragment after cleavage by Esp1 (Separase) or the form cut by TEV protease. Histone H3 is used as a loading control. Xrs2 levels do not change upon TEV induction. (C)

Example images of foci at *ARS607* before and after galactose-induced cleavage. Black circles highlight spot area in S phase cells and upon galactose-induction for 60 mins (TEV on). (D) Spot intensity profiles of SIM foci from experiments in Figure 6, $n \geq 35$. Full details and statistics are available in Table S4. (E) Quantitation of the percentage of frames containing 2 spots in movies ± TEV induction and a control strain that does not contain the galactose inducible TEV, $n \geq 10$. Full details and statistics are available in Table S4. Asterisks indicate a p value < 0.005.

Supplemental movie legend

Movie S1. Example movies of sister chromatid separation at induced DSBs, related to figure 7

Example movies of LacI-GFP spots located at the LacO array adjacent to the *MAT* locus. Movies are acquired and processed as described in Fig 7. Top row, left to right: wt S phase 37 °C uncut, wt S phase 37 °C cut 2h, *mcd1-1* S phase 37 °C uncut, *mcd1-1* S phase 37 °C cut 2h. Middle row: *rfa1-t11* S phase 37 °C uncut, *rfa1-t11* S phase 37 °C cut 2h, *rfa1-t11 mcd1-1* S phase 37 °C uncut, *rfa1-t11 mcd1-1* S phase 37 °C cut 2h. Bottom row: *rad50Δ* S phase 25 °C uncut, *rad50Δ* S phase 25 °C cut 2h. Scale bar = 2 µm.

Supplemental tables and table legends

Table S1 – Yeast strains and plasmids, related to figures 1-7 (included as an additional excel file)

Table S2 - Summary of peptide binding data (included as an additional excel file), related to figure 3

Table S3 - Cut efficiencies of strains used in experiments, related to figures 4,5,6,7

Table S4 – Summary of statistics of microscopy experiments (included as an additional excel file), related to figures 5, 6, 7

Table S3 - Cut efficiencies of strains used in experiments, related to figures 4,5,6,7

Strain	Relevant genotype	Temperature °C	Min after addition of galactose (HO induction)	% of intact MAT
GA6405	wild-type	30	0	100
			30	35 ± 14.36
			60	18 ± 3.08
			90	17 ± 3.9
GA6406	*rfa1-t11*	30	0	100
			30	32 ± 14.28
			60	22 ± 1.45
			90	16 ± 9.13
GA8858	wild-type	25	0	100
			120	23 ± 2.56
GA8256	*rad50Δ*	25	0	100
			120	21 ± 9.45
GA8569	*rfa1-t11*	25	0	100
			120	2 ± 1.44
GA8067	wild-type (untagged)	30	0	100
			120	21 ± 0.74
GA9194	*Scc1-3HA*	30	0	100
			120	18 ± 1.65
GA9241	*Scc1-3HA rad50Δ*	30	0	100
			120	10 ± 1.68
GA9246	*Scc1-3HA rfa1-t11*	30	0	100
			120	9 ± 0.62
GA8067	wild-type	25	0	100
			120	24 ± 2.1
GA9229	*mcd1-1*	25	0	100
			120	16 ± 0.89
GA9288	*mcd1-1 rfa1-t11*	25	0	100
			120	19 ± 1.25
GA9291	*mcd1-1 rad50Δ*	25	0	100
			120	1 ± 0.02
GA9247	*mcd1-1 rfa1-t11 rad50Δ*	25	0	100
			120	22 ± 2.3
GA8067	wild-type	37	0	100
			120	23 ± 1.3
GA9229	*mcd1-1*	37	0	100
			120	10 ± 0.56
GA9288	*mcd1-1 rfa1-t11*	37	0	100
			120	9 ± 1.82
GA9291	*mcd1-1 rad50Δ*	37	0	100
			120	24 ± 2.35
GA9247	*mcd1-1 rfa1-t11 rad50Δ*	37	0	100
			120	27 ± 2

Supplemental experimental procedures

Yeast strains and EMAP assay

The *rfa1-t11* allele was generated by transforming *NheI*-linearized plasmid *pKU2-rfa1-t11* into W303-1A (Soustelle et al., 2002). Cells were selected for the plasmid-borne *URA3* marker and plated on 5-fluoroorotic acid (5-FOA). The mutant was confirmed by sequencing and sensitivity to MMS and HU. Yeast strains were at grown at 30°C in YPAD media, unless stated differently. For experiments involving galactose driven induction of genes, yeast was grown in sterile filtered YPLGg media. Samples were always harvested in log phase cultures. EMAP was performed as in Hustedt *et al.,* 2015.

Drop tests and recovery assays

For drop assays, overnight cultures were diluted to a starting density of OD600 = 0.5 and serial 1:10 dilutions were plated on YPAD or the appropriate selective medium containing the indicated concentrations of MMS, HU or Zeocin. For liquid recovery or survival assays, overnight cultures were diluted to OD600 = 0.15 and grown for 3 h. Cultures were synchronized with α factor and were released into YPAD containing 0.2 M HU. After the indicated time points, relevant dilutions were plated onto YPAD and colonies were counted after 3 to 4 days. Recovery in (%) is the fraction of colonies at the indicated doses compared to the untreated control (0h) normalized to the survival of WT cells for each time point. Cut efficiency of the HO endonuclease at *MAT* was determined as in Horigome *et al.,* 2014, and reflects cleavage of both sisters, which have identical sequence. Primer sequences are available.

2D gels

Neutral/neutral 2D agarose gels were performed as described (Huberman et al., 1987; Wu and Gilbert, 1995). Genomic DNA was isolated from cells at a density of 5x106–1x107 from GA-4973, GA-5048, GA-

4971 and GA-4974 using a G-20 column (QIAGEN) followed by digestion with *Pst*I. Genomic DNA was separated on a 0.4% agarose gel in TBE for 40 h at 0.6 V/cm in the first dimension and on a 1.2% agarose gel in TBE at 3 V/cm for 18 h. Replication intermediates at ARS607 were detected after Southern blotting and hybridization with a DIG-labeled probe. The relative ratio of fork firing is expressed as signal of bubble arc to the amount of 1N linear fragments, normalized to wild-type.

DNA combing

Dynamic molecular combing was performed as described previously (Michalet et al., 1997; Tourriere et al., 2005). Wild-type (GA-5382), *rfa1-t11* (GA-5383), *mec1-100* (GA-5385), and *rfa1-t11 mec1-100* (GA-5386) were arrested in G1. 20 min before release into S phase 0.4 mg/ml IdU were added. Cells were incubated for 90 min in YPAD containing 0.2 M HU and 0.4 mg/ml IdU, then washed and released into fresh YPAD in presence of 0.4mg/ml CldU for additional 90 min. IdU and CldU were detected with anti-BrdU antibodies (BD44-Becton Dickinson and BU1/75-AbCys, respectively). Due to cross-reaction of the IdU- and CldU-specific antibodies, both channels are shown together as “replicated fiber fraction” (green/white channels Fig. 2D). DNA molecules were counter-stained with an anti-DNA antibody (MAB3034, Chemicon) and an anti-mouse IgG coupled to Alexa 647 (Molecular Probes). A Leica DM6000B microscope was used to record the images, which were processed as described (Pasero et al., 2002). DNA fibers from 4 independent experiments were analyzed using MetaMorph. R was used for statistical analysis. Each experiment was checked for batch effects, before all DNA fibers per strain were pooled and analyzed by a paired Wilcox test. DNA fibers analyzed from *rfa1-t11*, *mec1-100* and *rfa1-t11 mec1-100* cells were significantly different from wild-type cells ($P<0.05$).

Co-immunoprecipitation (Pulldown) and Chromatin immunoprecipitation (ChIP)

ChIP was performed as described in Cobb et al., 2003. G1-synchronized cells were released into 0.2 M HU-containing media at 30 °C for approximately 1 h and fixed with 1% formaldehyde at the indicated

time points. Monoclonal anti-HA was used to precipitate HA-tagged DNA pol α. Cell extracts were incubated with BSA-saturated Dynabeads coupled to anti-HA antibody for 2 h at 4 °C. As a background control we used BSA-coupled Dynabeads without antibody. Real-time PCR was used for amplification of the precipitated DNA regions. Sequences for the primers/probes that amplify regions in the *S. cerevisiae* genome correspond to ARS607, a site 14 kb away from ARS607 and ARS501 as described in (Cobb et al., 2003). For quantification, Applied Biosystems 7500 Fast Real-time PCR System and software was used. The data for each strain are the average of 3 independent experiments with real-time PCR performed in duplicate (standard error of the mean is indicated by the error bars). Absolute fold enrichment at ARS607 or ARS501 was calculated for each time point as follows: the signal from the anti-HA-coupled Dynabeads was divided by the signal from the BSA-coated Dynabeads, after both signals were first normalized to the signal from input DNA. Relative enrichment at ARS607 or ARS501 was obtained by normalizing the absolute enrichment at ARS607 or ARS501 to the absolute enrichment at a locus 14 kb away from ARS607.

Co-immunoprecipitations were done as in (Hustedt et al., 2015) with the following modifications: Roche complete protease inhibitor tablets (Sigma 04693116001) were used at double the recommended concentration to prevent Rad50 degradation and phosphatase inhibitors were not added. 1250 units of Benzonase (Sigma E1014) was added for 30 min on ice after bead beating to digest both RNA and DNA. Since Rfa1 bound non-specifically to beads a stringent wash was used consisting of: 10 mM Tris PH 8.0, 500 mM LiAC, 0.2% NP-40, 0.5% Na-deoxycholate, 1 mM EDTA. Washes were done 3 x 5mins at 4 °C using a circular shaker set to 750 rpm.

Western blotting and antibodies

Western blotting of TCA precipitated proteins separated on a SDS-PAGE gel (Invitrogen) was performed as in (Seeber et al., 2013). Transfer was done using Biorad Turbo blot system onto PVDF membranes.

Anti-actin was from Millipore (#MAB1501) and anti-Mcm2 was purchased from Santa Cruz (#6680). Rad53 protein was detected using a custom-made mouse monoclonal antibody (GenScript) against the FHA2 domain of Rad53. Anti-γH2A is a custom-made monoclonal antibody that is specific for phospho-S129 in yeast H2A. Anti-Rfa1 is a polyclonal antibody raised against purified yeast RPA consisting of all three subunits and was purchased from Agrisera (#AS07214). Anti-PK was purchased from Acris antibodies (#SM1691). Anti-Mre11 is a rabbit polyclonal antibody (kind gift of John Petrini; Sloan Kettering Memorial Hospital, #59567). Monoclonal anti-HA 12CA5 was from Santa Cruz (#sc-57592).

Yeast two hybrid analyses

Two-hybrid analyses were performed using galactose inducible bait and prey as described (Bjergbaek et al., 2005). The lacZ reporter pSH18-34, the bait and the prey were transformed into EGY191 cells (GA-1211). After glucose depletion, 2% galactose was added to the exponentially growing culture to induce the fusion proteins. The β-galactosidase assay for permeabilized cells was used to detect and quantify protein-protein interactions. Four independent transformants were analyzed in two or more independent experiments. Western blot analysis was used to check the expression of the fusion proteins (data not shown). B-galactosidase units are defined as OD420/(OD600*dilution*time(min)).

FACS analysis

For FACS, cultures were grown as for Western blotting. A 1 ml sample was taken for each time-point and was spun down and fixed in 70% ethanol and stored at 4 °C. When ready for analysis samples were sedimented and resuspended in 50 mM Tris-HCL pH 7.5 + 200 µg/ml RNase A and digested for 2 h at 37 °C. Samples were then sedimented and resuspended in 50 mM Na-Citrate pH 7.0 + 10 µg/ml PI. Samples were stained overnight at 4 °C. The following morning the samples were briefly sonicated and diluted in more Na-Citrate + PI. Samples were measured on a Becton Dickinson FACS Calibur and at least 10 000 cells were measured.

Protein expression and purification

Budding yeast Rfa1-t11$_{1-132}$ was cloned into pOPINF vector using the In-Fusion system (Clontech) (Berrow et al., 2007) and expressed in *E. coli* B834s cells (Novagen) grown in seleno-methionine-supplemented medium (Molecular Dimensions). Recombinant protein was affinity purified via an N-terminal $(His)_6$ tag using Ni^{2+}-NTA Superflow (Qiagen) according to manufacturer's instructions. The $(His)_6$ tag was removed by HRV 3C protease digestion and the protein was further purified by anion exchange using 1ml HiTrap Capto Q column (GE Healthcare) followed by gel filtration on a HiLoad 16/60 Superdex 75 column (GE Healthcare) in 20 mM Tris pH 8.0, 150 mM NaCl, 0.02% NaN3 and 1 mM TCEP. The purified protein was concentrated to 20 mg/ml, flash-frozen in liquid N_2 and stored at -80°C.

Peptides and peptide microarray

Scanning peptide array was designed to cover all of MRX excluding the coiled-coil domains of Rad50, using 18 amino acids long peptides with 9 amino acid overlap. Peptides were synthesized and spotted onto a glass slide by JPT Peptide Technologies GmbH according to the PepStar microarray protocol. Rfa1 and *rfa1-t11* purified peptides where incubated on the peptide glass slide at a concentration of 0.3 mg/ml in a humid chamber at 4 °C for 1 hour. The peptide slide was then washed 5x5 times in TBS-Buffer + 0.1% Tween20 (TBS-T) with gentle agitation. Next, the secondary Rfa1 antibody was incubated at a 1:10000 dilution in TBS-T with the slide for 1 h at 4 °C. The slide was washed as above. The fluorescent Alexa antibodies (Alexa647 anti-rabbit against the Rfa1 antibody and Alexa555 anti-mouse for the IgG control) were used at a 1:10000 dilution and incubated as above. Slide was then washed again as in the previous step followed by 5x5 min washes in deionized water. All solutions were filtered with a 0.2 µm filter. The slide was dried with a stream of air and immediately scanned with a Zeiss Axioimager Z1 microscope. Images were stitched using Zen Blue software and analysis was done using the protein array analyzer plugin for Fiji (ImageJ) (Carpentier and Henault, 2010).

N-terminal Cy5-labeled peptides of *S. cerevisiae* Rad50 (^{145}-VPKAILEYVIFCHQEDSL-^{162}; ^{163}-WPLSEPSNLKKKFDEIFQ-^{180}; ^{1171}-IRSDEVSSTVKGKSYNYR-^{1188}) and *S. cerevisiae* Mre11 (^{82}-DKPCELELLSDPSQVFHY-^{99}; ^{118}-VFGISGNHDDASGDSLLC-^{135}; ^{136}-PMDILHATGLINHFGKVI-^{153}) were purchased from JPT Peptide Technologies (Berlin, Germany). Peptides were dissolved in 0.1 M Tris pH 8.0 and stored as 4 mM stock solutions at -80^{0}C until use.

Microscale thermophoresis (MST)

Experiments were carried out in 20 mM Tris buffer pH 8.0 containing 150 mM NaCl, 0.05 % Tween-20 and 0.5 mg/ml BSA. Purified *S. cerevisiae* Rfa1-N (residues 1-132) and Cy5-labeled Rad50 and Mre11 peptides were centrifuged at 13200 *g* for 5 min at room temperature prior to the assays. A dilution series of Rfa1-N yielding 14 different protein concentrations starting from 0.12 µM to 1000 µM was mixed separately with labeled Rad50 and Mre11 peptides at a fixed concentration of 25 µM. After 15 min incubation at room temperature, followed by centrifugation at 5000 *g* for 5 min, approximately 4 µL of each solution was filled into Monolith NT Premium Coated Capillaries (NanoTemper Technologies GmbH). Thermophoresis was measured using a Monolith NT.115 instrument (NanoTemper Technologies GmbH) at 23°C with 5 s / 30 s / 5 s laser off/on/off times, respectively. Instrument parameters were adjusted to 1-20 % LED power and 20 % MST power. Data of three independently pipetted measurements were analyzed (NT Analysis software version 1.5.41, NanoTemper Technologies GmbH) using the signal from thermophoresis and plotted using GraphPad Prism version 6.01 (La Jolla, CA, USA).

Name	Sequence	Protein	K_d ± SEM (µM)
VPK	VPKAILEYVIFCHQEDSL	Rad50	63.6 ± 7
DKP	DKPCELELLSDPSQVFHY	Mre11	n.d.
IRS	IRSDEVSSTVKGKSYNYR	Rad50	n.d.
VFG	VFGISGNHDDASGDSLLC	Mre11	n.d.
WPL	WPLSEPSNLKKKFDEIFQ	Rad50	n.d.
PMD	PMDILHATGLINHFGKVI	Mre11	n.d.

Crystallization

Crystals of Rfa1-t11$_{1-132}$ were grown at 20 °C using the sitting-drop vapor diffusion method after mixing 0.1 µl of Rfa1-t11$_{1-132}$ (20 mg/ml in 20 mM Tris pH 8.0, 150 mM NaCl, 0.02% NaN3 and 1 mM TCEP) with 0.1 µl of reservoir containing 200 mM ammonium fluoride and 20% (w/v) PEG 3350. Crystals were transferred into a cryo-solution (20 mM Tris pH 8.0, 150 mM NaCl, 200 mM ammonium fluoride, 20% (w/v) PEG 3350, 24 % (v/v) ethylene glycol) and flash frozen in liquid N2 for data collection. Diffraction data were collected at the Swiss Light Source, Paul Scherrer Institut, Villigen, Switzerland.

Structure determination and model building

Reflection data were indexed, integrated, and scaled using XDS (Kabsch, 2010). The structure of Rfa1-t11$_{1-132}$ was solved using the AutoSol pipeline implemented in the PHENIX package via SAD, using four seleno-methionine sites per molecule (Adams et al., 2010). The initial AutoSol structural model was manually completed and refined by the crystallographic simulated annealing routine followed by individual B-factor refinement in PHENIX. The final model was obtained after several cycles of manual rebuilding in COOT (Emsley et al., 2010) followed by refinement rounds in PHENIX and BUSTER (Bricogne et al, 2010). The Rfa1-t11$_{1-132}$ structure was validated using Molprobity (Chen et al., 2010) and COOT. Structural images for Figure 1B were prepared with PyMOL (DeLano Scientific; http://pymol.sourceforge.net/). Data collection and refinement statistics are found in Table 1.

DSB end separation assay

The DSB end separation assay was performed as in (Lobachev et al., 2004).

Microscopy

Live microscopy used an Olympus IX81 microscope equipped with a Yokogawa CSU-X1 scan head, an EM-CCD Cascade II (Photometrics), a ASI MS-2000 Z-piezo stage and a PlanApo x100, NA 1.45 total

internal reflection fluorescence microscope oil objective. Fluorophores were excited at 567 nm (mCherry, ~30 μW), 515 nm (YFP, ~65 μW) and 491 (GFP, ~75 μW). Time-lapse series (1 min) of 8 optical slices per stack were streamed for 750 timepoints. Live cell cultures were imaged for a maximum of 60 minutes. Fixation of cells was done using 4% PFA for 1 min followed by washing 3x and then resuspending the cells in PBS. Mre11-YFP and cohesin spot separation experiments of fixed cells were acquired using 50 ms exposures of 50 slices with 0.2 μm intervals. For experiments where the DSB was marked on either side of the break 100 ms exposures were used with 50 slices at 0.2 μm intervals. Images were deconvolved and where necessary, channel aligned, using Huygens Pro.

Microarray slides were scanned with a Zeiss Axioimager Z1 microscope with a Plan-APOCHROMAT 10x/0.45 M27 objective lens and either Alexa555 or Alexa647 filter. The light source used was an X-Cite 120 EXFO Metal Halide lamp and images were detected on an Axiocam 506 camera. 50 ms exposures were used for the Alexa555 signal and 100 ms exposures for the Alexa647 signal. 120 tiles were taken, covering the whole peptide array and then stitched together using Zen Blue software.

Structured illumination images were acquired on a Zeiss Elyra S.1 microscope with a Andor iXon 885 EMCCD camera using a HR diode 488 100nW solid state laser, BP 525-580 + LP 750 filter and a PLAN-APOCHROMAT 63x N.A. 1.4 oil DIC objective lens. Cells were fixed to a glass slide using Concanavalin A and a thin SIM grade Zeiss 1.5 glass coverslip was used while imaging. Cells were fully sectioned by 50 slices with 0.1 nm intervals taken at 50 ms exposures per slice using 5 rotations of the illumination grid. Brightfield images of the cells were also acquired using an X-Cite PC 120 EXFO Metal Halide lamp. Zen Black was used to process the images using automatic settings but retaining the raw scale.

Spot volume analysis

Spot volumes were determined by first creating a maximum intensity projection of the acquired 3D SIM stack. Fiji (ImageJ) was then used to segment the images to allow for easy particle detection and

determination of both area and mean intensity of each particle. Particle detection and segmentation was done using the same setting for all images. The detected particles where then overlaid on the corresponding bright field images to allow for cell cycle phase determination.

Spot separation movie analysis

Time lapse movies were maximum intensity projected and spot separation was measured in the X and Y dimensions using the Fiji spot tracking plugin Trackmate (Jaqaman et al., 2008) with the following settings: Differences of Gaussian (DoG) detector with estimated blob diameter 0.3 µm, sub-pixel localization enabled, LAP tracker with frame to frame linking, segment gap closing (maximum frame gap of 20 frames), track segment splitting and track segment merging set to maximum distances of 0.5 µm. Length of splitting evens were analyzed using a custom Fiji script available on request.

Supplemental references

Adams, P.D., Afonine, P.V., Bunkoczi, G., Chen, V.B., Davis, I.W., Echols, N., Headd, J.J., Hung, L.W., Kapral, G.J., Grosse-Kunstleve, R.W*., et al.* (2010). PHENIX: a comprehensive Python-based system for macromolecular structure solution. Acta crystallographica Section D, Biological crystallography *66*, 213-221.

Berrow, N.S., Alderton, D., Sainsbury, S., Nettleship, J., Assenberg, R., Rahman, N., Stuart, D.I., and Owens, R.J. (2007). A versatile ligation-independent cloning method suitable for high-throughput expression screening applications. Nucleic Acids Res *35*, e45.

Bjergbaek, L., Cobb, J.A., Tsai-Pflugfelder, M., and Gasser, S.M. (2005). Mechanistically distinct roles for Sgs1p in checkpoint activation and replication fork maintenance. Embo J *24*, 405-417.

Carpentier, G., and Henault, E. (2010). Protein Array Analyzer for ImageJ. Proceedings of the ImageJ User and Developer Conference, pp. 238-240.

Chen, V.B., Arendall, W.B., 3rd, Headd, J.J., Keedy, D.A., Immormino, R.M., Kapral, G.J., Murray, L.W., Richardson, J.S., and Richardson, D.C. (2010). MolProbity: all-atom structure validation for macromolecular crystallography. Acta crystallographica Section D, Biological crystallography *66*, 12-21.

Cobb, J.A., Bjergbaek, L., Shimada, K., Frei, C., and Gasser, S.M. (2003). DNA polymerase stabilization at stalled replication forks requires Mec1 and the RecQ helicase Sgs1. Embo j *22*, 4325-4336.

Cobb, J.A., Schleker, T., Rojas, V., Bjergbaek, L., Tercero, J.A., and Gasser, S.M. (2005). Replisome instability, fork collapse, and gross chromosomal rearrangements arise synergistically from Mec1 kinase and RecQ helicase mutations. Genes Dev *19*, 3055-3069.

Dion, V., Kalck, V., Seeber, A., Schleker, T., and Gasser, S.M. (2013). Cohesin and the nucleolus constrain the mobility of spontaneous repair foci. EMBO Rep *14*, 984-991.

Dubrana, K., van Attikum, H., Hediger, F., and Gasser, S.M. (2007). The processing of double-strand breaks and binding of single-strand-binding proteins RPA and Rad51 modulate the formation of ATR-kinase foci in yeast. J Cell Sci *120*, 4209-4220.

Emsley, P., Lohkamp, B., Scott, W.G., and Cowtan, K. (2010). Features and development of Coot. Acta crystallographica Section D, Biological crystallography *66*, 486-501.

Golemis, E.A., Serebriiskii, I., Finley, R.L., Jr., Kolonin, M.G., Gyuris, J., and Brent, R. (2011). Interaction trap/two-hybrid system to identify interacting proteins. Current protocols in neuroscience / editorial board, Jacqueline N Crawley [et al] *Chapter 4*, Unit 4.4.

Hegnauer, A.M., Hustedt, N., Shimada, K., Pike, B.L., Vogel, M., Amsler, P., Rubin, S.M., van Leeuwen, F., Guenole, A., van Attikum, H*., et al.* (2012). An N-terminal acidic region of Sgs1 interacts with Rpa70 and recruits Rad53 kinase to stalled forks. Embo j *31*, 3768-3783.

Heun, P., Laroche, T., Shimada, K., Furrer, P., and Gasser, S.M. (2001). Chromosome dynamics in the yeast interphase nucleus. Science *294*, 2181-2186.

Huberman, J.A., Spotila, L.D., Nawotka, K.A., el-Assouli, S.M., and Davis, L.R. (1987). The in vivo replication origin of the yeast 2 microns plasmid. Cell *51*, 473-481.

Hustedt, N., Seeber, A., Sack, R., Tsai-Pflugfelder, M., Bhullar, B., Vlaming, H., van Leeuwen, F., Guenole, A., van Attikum, H., Srivas, R*., et al.* (2015). Yeast PP4 interacts with ATR homolog Ddc2-Mec1 and regulates checkpoint signaling. Mol Cell *57*, 273-289.

Jaqaman, K., Loerke, D., Mettlen, M., Kuwata, H., Grinstein, S., Schmid, S.L., and Danuser, G. (2008). Robust single-particle tracking in live-cell time-lapse sequences. Nature methods *5*, 695-702.

Lee, S.E., Moore, J.K., Holmes, A., Umezu, K., Kolodner, R.D., and Haber, J.E. (1998). Saccharomyces Ku70, mre11/rad50 and RPA proteins regulate adaptation to G2/M arrest after DNA damage. Cell *94*, 399-409.

Lobachev, K., Vitriol, E., Stemple, J., Resnick, M.A., and Bloom, K. (2004). Chromosome fragmentation after induction of a double-strand break is an active process prevented by the RMX repair complex. Curr Biol *14*, 2107-2112.

Ma, J.L., Kim, E.M., Haber, J.E., and Lee, S.E. (2003). Yeast Mre11 and Rad1 proteins define a Ku-independent mechanism to repair double-strand breaks lacking overlapping end sequences. Mol Cell Biol *23*, 8820-8828.

Michalet, X., Ekong, R., Fougerousse, F., Rousseaux, S., Schurra, C., Hornigold, N., van Slegtenhorst, M., Wolfe, J., Povey, S., Beckmann, J.S*., et al.* (1997). Dynamic molecular combing: stretching the whole human genome for high-resolution studies. Science *277*, 1518-1523.

Pasero, P., Bensimon, A., and Schwob, E. (2002). Single-molecule analysis reveals clustering and epigenetic regulation of replication origins at the yeast rDNA locus. Genes Dev *16*, 2479-2484.

Seeber, A., Dion, V., and Gasser, S.M. (2013). Checkpoint kinases and the INO80 nucleosome remodeling complex enhance global chromatin mobility in response to DNA damage. Genes Dev *27*, 1999-2008.

Soustelle, C., Vedel, M., Kolodner, R., and Nicolas, A. (2002). Replication protein A is required for meiotic recombination in Saccharomyces cerevisiae. Genetics *161*, 535-547.

Tourriere, H., Versini, G., Cordon-Preciado, V., Alabert, C., and Pasero, P. (2005). Mrc1 and Tof1 promote replication fork progression and recovery independently of Rad53. Mol Cell *19*, 699-706.

Wu, J.R., and Gilbert, D.M. (1995). Rapid DNA preparation for 2D gel analysis of replication intermediates. Nucleic Acids Res *23*, 3997-3998.